nature communications

Article

https://doi.org/10.1038/s41467-024-50888-8

Structural basis of the obligatory exchange mode of human neutral amino acid transporter ASCT2

Received: 16 November 2023

Accepted: 23 July 2024

Published online: 03 August 2024

Check for updates

Anna M. Borowska[1], Maria Gabriella Chiariello[2], Alisa A. Garaeva[1,4], Jan Rheinberger[1,3], Siewert J. Marrink[2], Cristina Paulino[1,3] ✉ & Dirk J. Slotboom[1] ✉

ASCT2 is an obligate exchanger of neutral amino acids, contributing to cellular amino acid homeostasis. ASCT2 belongs to the same family (SLC1) as Excitatory Amino Acid Transporters (EAATs) that concentrate glutamate in the cytosol. The mechanism that makes ASCT2 an exchanger rather than a concentrator remains enigmatic. Here, we employ cryo-electron microscopy and molecular dynamics simulations to elucidate the structural basis of the exchange mechanism of ASCT2. We establish that ASCT2 binds three Na^+ ions per transported substrate and visits a state that likely acts as checkpoint in preventing Na^+ ion leakage, both features shared with EAATs. However, in contrast to EAATs, ASCT2 retains one Na^+ ion even under Na^+-depleted conditions. We demonstrate that ASCT2 cannot undergo the structural transition in TM7 that is essential for the concentrative transport cycle of EAATs. This structural rigidity and the high-affinity Na^+ binding site effectively confine ASCT2 to an exchange mode.

Amino acid homeostasis in the cytosol and blood plasma is fundamental for human physiology[1]. Secondary active transporters in the plasma membrane play a central role in maintaining the necessary amino acid concentrations. Driven by the Na^+ electrochemical gradient, concentrative transporters accumulate amino acids in the cytosol. Exchangers may subsequently use the imported amino acid to bring in a low-abundant amino acid through an antiport process. The dominant exchange transporter for neutral amino acids is ASCT2, which has gained interest because of its overexpression in many cancer cell types[2–6]. ASCT2 mediates the efflux of polar amino acids in exchange for glutamine, a critical precursor for cancer cell proliferation and tumor growth. Consequently, ASCT2 emerged as a potential drug target for anticancer therapy.

ASCT2 belongs to the solute carrier 1A (SLC1A) family of membrane transporters, which in humans also includes the related exchanger ASCT1 and five subtypes of excitatory amino acid transporters (EAAT1–5)[7]. The SLC1A family also has homologs in prokaryotes, of which the archaeal Glt_{Tk} and Glt_{Ph} are well characterized. Multiple structures of EAATs (EAAT1, EAAT2, EAAT3)[8–13], ASCTs (ASCT1 and ASCT2)[14–18], Glt_{Tk}[19–21] and Glt_{Ph}[22–26] have been determined by X-ray crystallography and single particle cryo-electron microscopy (cryo-EM) over the past two decades, providing insight into the structural basis of transport. SLC1A transporters share a homotrimeric structure[27] (Supplementary Fig. 1a), where each protomer operates as an independent functional unit[28,29]. Protomers consist of scaffold and transport domains, with the scaffold domains mediating protomer-protomer interactions. Transport domains at the periphery of the trimer bind and encapsulate the coupling ions and the amino acid substrate. A key structural element is the helical hairpin 2 (HP2), consisting of two antiparallel α-helices (HP2a and HP2b) connected by a loop, which acts as a gate of the substrate binding pocket. The closure of the HP2 loop is a prerequisite for the transport domain to undergo

[1]Faculty of Science and Engineering, Groningen Biomolecular Sciences and Biotechnology, Membrane Enzymology Group, University of Groningen, Groningen, the Netherlands. [2]Faculty of Science and Engineering, Groningen Biomolecular Sciences and Biotechnology Institute, Molecular Dynamics Group, University of Groningen, Groningen, the Netherlands. [3]Biochemistry Center Heidelberg, Heidelberg University, Heidelberg, Germany. [4]Present address: Institute of Medical Microbiology, University of Zurich, Zurich, Switzerland. ✉e-mail: cristina.paulino@bzh.uni-heidelberg.de; d.j.slotboom@rug.nl

conformational movements relative to the scaffold domain, which ultimately results in an elevator-like motion that moves the substrate binding site across the membrane (Supplementary Fig. 1a). The HP2 loop controls substrate binding and release on both sides of the membrane, defining the mechanism for amino acid transport as a one-gate elevator[15].

Although ASCTs, EAATs, and archaeal homologs Glt_{Tk} and Glt_{Ph} share many structural and mechanistic similarities, there are notable differences in their transport mode. EAATs, Glt_{Tk}, and Glt_{Ph} are concentrative transporters, mediating the accumulation of acidic amino acids in the cytosol, while ASCTs are obligate amino acid exchangers. The archaeal transporters Glt_{Tk} and Glt_{Ph} couple the uptake of aspartate to co-transport of three Na^+ ions[30] (Supplementary Fig. 1b). Human EAATs have a more complex transport mechanism since the uptake of one glutamate molecule is coupled to co-transport of three Na^+ ions and an H^+ ion, followed by a counter-transport of a K^+ ion[31,32] (Supplementary Fig. 1b). By contrast, ASCTs mediate a Na^+-dependent amino acid exchange rather than an accumulation, meaning the transport of amino acid substrate and Na^+ ions is coupled to the counter-transport or antiport of another amino acid and Na^+ ions[33,34] (Supplementary Fig. 1b).

Earlier structural and computational studies demonstrate a high level of cooperativity in the binding and release of the substrate and co-transported ions in concentrative transporters[20,23,24,35–39]. The closure of the HP2 loop is possible when both the substrate and co-transported ions (Na^+ and H^+ in EAATs) are present or when nothing (in prokaryotic members) or only a K^+ ion (in EAATs) is bound to the transport domain[39] (Supplementary Fig. 1c). Consequently, proper closure of the HP2 loop is hindered when the transport domain is only partially occupied with Na^+ ions. Notably, the conformation of HP2 closely correlates with another critical structural element, namely that of the conserved NMDG motif found in the central region of TM7, which is directly influenced by the binding of Na^+ ions[19,21,23,25,40,41]. For concentrators, the NMDG region adopts a non-compact, extended conformation in the absence of bound Na^+ ions (Supplementary Fig. 1c). Here, the central methionine residue of the NMDG motif points away from the Na^+ binding sites, effectively destroying the coordination of Na^+ ions. This extended state occurs when the binding sites face the cytosol in the inward-oriented state, where the Na^+ concentration is low (~20 mM)[42]. The HP2 loop can close in this extended state, and the transport domain (devoid of its amino acid substrate and Na^+ ions but additionally bound to K^+ ion in EAATs) can reorient from the inward- to the outward-facing state, exposing the binding sites to a high Na^+ concentration (~140 mM). In this outward-facing state, Na^+ binding occurs once the extended NMDG region adopts a compact conformation, which creates two specific sites (Na1 and Na3). The binding of Na^+ then stabilizes the compact conformation in a conformational selection process[19,40]. In the Na^+-bound conformation, the methionine of the NMDG motif points towards the center of the transport domain (Supplementary Fig. 1c). While the binding of Na^+ ions stabilizes this compact conformation of the NMDG motif, it also restricts the closure of the HP2 loop and the elevator movement, effectively preventing an uncoupled leak of Na^+ ions. With the Na^+ ions bound to positions Na1 and Na3, subsequent binding of the amino acid and the last Na^+ ion to Na2 can occur, allowing for the closure of the HP2 gate and the transmembrane elevator movement of the transport domain (Supplementary Fig. 1c). As a result, concentrative transporters exhibit a strictly coordinated interplay between the conformation of the conserved NMDG motif and HP2 rearrangement, allowing them to reorient the empty (in archaeal homologs) or K^+-bound (in EAATs) transport domain. Despite substantial similarities in sequence, structural assembly, transport mechanism, and cation dependency, the existing structural and functional models of concentrative transporters have been unable to unravel the Na^+ and substrate coupling mechanism and its relation to the exchange mode in ASCTs.

In this work, we aim to uncover the structural basis of the Na^+ and substrate coupling mechanism in the obligatory exchanger ASCT2. Using cryo-EM, we obtained structures of ASCT2 at high Na^+ concentrations and under Na^+-depleted conditions. The cryo-EM analysis at high Na^+ concentration revealed that the binding of one substrate molecule is coupled to three Na^+ ions. When we depleted ASCT2 from Na^+ ions, the transporter retained the compact NMDG conformation and displayed one Na^+ ion bound at the Na1 binding site. Moreover, unbiased molecular dynamics (MD) simulations showed that ASCT2 does not undergo a structural transition in the TM7 region, which, unless bound to the substrate and Na^+ ions, hinders HP2 closure and the elevator movement, thereby effectively locking the transporter in an exchange mode. We further found an intermediate state that might serve as a checkpoint for the transport domain movements across the membrane, limiting the conformational transition from outward to inward-facing state without substrate, thus preventing Na^+ ions from leaking.

Results

Amino acid transport mediated by ASCT2 strictly depends on Na^+ ions

We monitored the Na^+ dependence of purified ASCT2 using a proteoliposome-based counterflow assay. The assay measures the exchange of luminal unlabeled glutamine for external radiolabeled glutamine. ASCT2 showed robust glutamine transport when Na^+ ions were present on both sides of proteoliposomes (Fig. 1a). Consistent with the Na^+ dependence of transport[14], substitution of Na^+ ions with K^+ ions in the external buffer completely abolished amino acid exchange, regardless of whether the luminal buffers contained Na^+ or K^+. Unexpectedly, we observed that by replacing Na^+ ions with K^+ ions in the luminal buffer while keeping Na^+ ions in the external buffer, ASCT2 exhibited slow uptake of radiolabeled glutamine. This observation can be explained because a minimal yet sufficient accumulation of Na^+ ions occurs inside the liposomes through half transport cycles of reconstituted ASCT2. With an average of 50 protein trimers reconstituted in proteoliposomes with 400 nm diameter, these half cycles will collectively allow 150, 300, or 450 Na^+ ions to enter the liposomes (assuming that 1, 2 or 3 Na^+ are released in the half cycle, respectively), resulting effectively in a Na^+ ion concentration of 60-180 μM. This concentration is apparently sufficient for a few ASCT2 proteins to bind substrate and Na^+ ions again and reorient to the external side of the liposomes. Consequently, we observed a slow increase in glutamine captured in the liposomes, even in the initial absence of internal Na^+ ions. These findings align with previous data[43], showing the essential role of Na^+ ions in facilitating amino acid exchange by ASCT2 across the lipid bilayer. Next, we aimed to uncover the structural basis of the Na^+ and substrate coupling mechanism in the exchanger ASCT2 using cryo-EM.

ASCT2 adopts an outward-facing conformation in lipid nanodiscs

Previously, eight structures of ASCT2 were solved using cryo-EM[14–17]. However, none of these structures provided the resolution needed to discern bound cations to the transport domain. Therefore, we set out to obtain a higher-resolution cryo-EM structure. We reconstituted ASCT2 in lipid nanodiscs using the membrane scaffold protein 2N2 (MSP2N2). To evaluate the quality of the preparations and increase the chance of achieving a high-resolution reconstruction during single particle analysis, we assessed the homogeneity of the nanodisc assemblies formed at different lipid-to-protein ratios (Supplementary Fig. 2a). Size-exclusion chromatography revealed that a molar ratio of 1:5:70 (ASCT2 trimer to MSP to lipids) yielded the most homogeneous preparations. Subsequently, we collected cryo-EM data of ASCT2 under saturating conditions in the presence of 200 mM Na^+ and 1 mM glutamine. After refinement with imposed C3 symmetry, we obtained a

https://doi.org/10.1038/s41467-024-50888-8

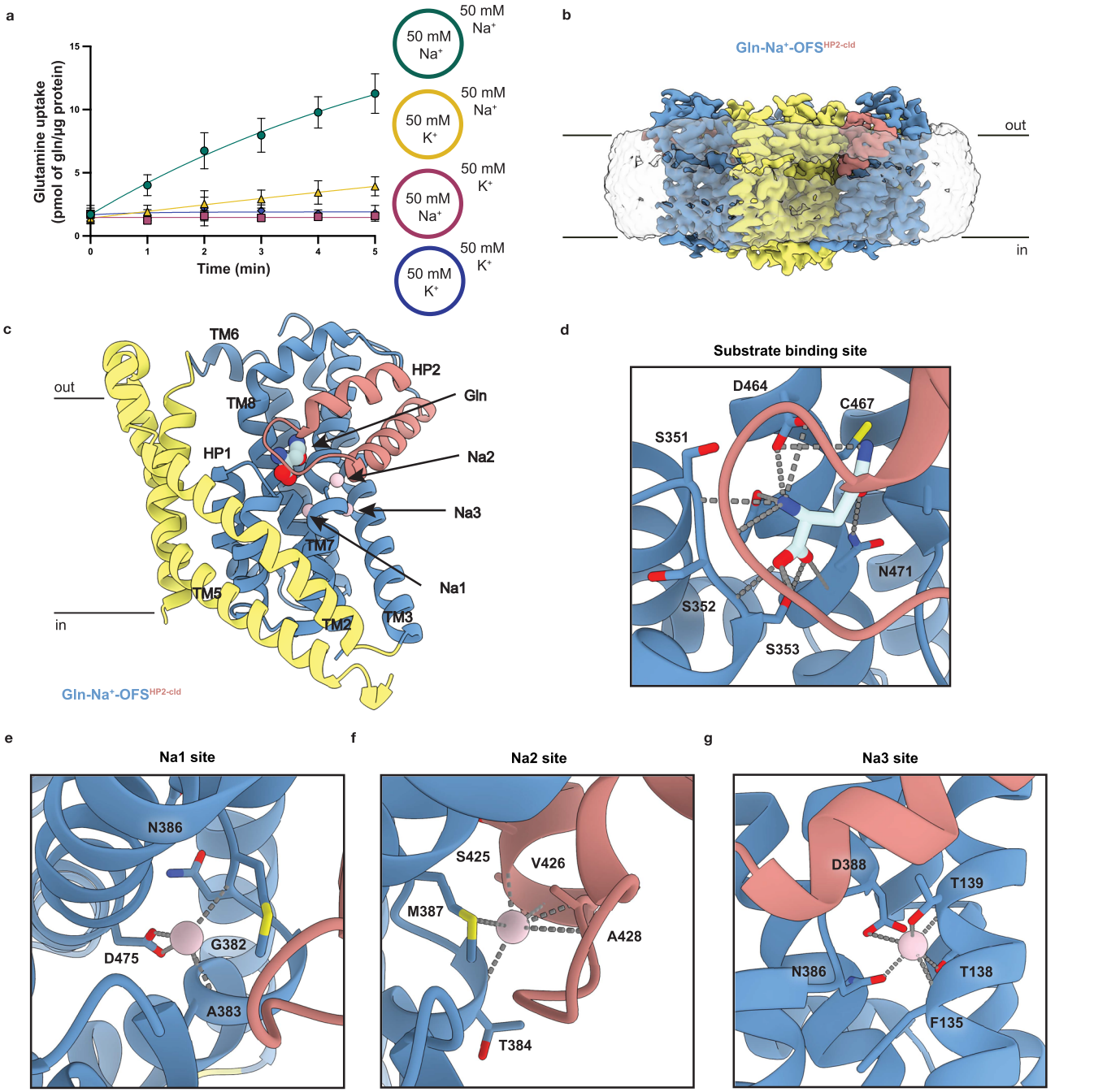

Fig. 1 | Cryo-EM structure of ASCT2 in lipid nanodiscs in the presence of Na^+ and glutamine. a Impact of Na^+ ions on glutamine transport mediated by ASCT2 measured in a radioactive uptake assay at indicated salt conditions. Data show the exchange of glutamine in the presence of internal and external Na^+ ions (green circles); exchange of glutamine with internal K^+ ions and external Na^+ ions (yellow triangle); exchange of glutamine with internal Na^+ ions and external K^+ ions (pink square); and exchange of glutamine in the presence of internal and external K^+ ions (blue diamond). Data points and error bars represent mean values ± SEM from $n = 2$ biologically independent experiments, each done in two or three technical replicates. Source data are provided as a Source Data file. **b** Cryo-EM map of trimeric ASCT2 in lipid nanodiscs in the presence of Na^+ ions and glutamine in an outward-facing state with closed HP2 gate (Gln-Na^+-$OFS^{HP2\text{-}cld}$) at 2.6 Å resolution, countered at 5σ. Each protomer is colored according to respective domains: scaffold domain in yellow, transport domain in blue, and HP2 region in salmon. The surrounding nanodisc is shown as a transparent unsharpened map at a lower countered level (3.7σ). The view is shown from the membrane side and the membrane boundaries are indicated as lines. **c** The cryo-EM structure of one ASCT2 protomer in the outward-occluded state (Gln-Na^+-$OFS^{HP2\text{-}cld}$). The scaffold domain is colored in yellow and the transport domain in blue. The closed HP2 gate is displayed in salmon, while glutamine and Na^+ ions are in light cyan and pink, respectively. The membrane boundaries are indicated as lines. **d** Close-up view of the substrate binding pocket highlighting the interactions between glutamine (light cyan) and the transport domain with the coordinating displayed as sticks. **e**–**g** A close-up view of the Na^+ ions (pink) bound at Na1 (**e**), Na2 (**f**), and Na3 (**g**) sites with displayed coordinating residues.

reconstruction of ASCT2 at a resolution of 2.6 Å (Fig. 1b, Supplementary Figs. 3 and 4a, Supplementary Table 2). All three protomers adopt the outward-facing occluded conformation (referred to as Gln-Na^+-$OFS^{HP2\text{-}cld}$ state), which is virtually identical to the previously determined conformation in the presence of a Fab fragment in detergent solution (r.m.s.d. of Cα atoms 0.918 Å)[16] (Supplementary Fig. 2b). The high-resolution cryo-EM map allowed a confident assignment of the ligand and ions bound to ASCT2 (Fig. 1c).

Three Na^+ ions bind with glutamine during the transport domain movement

In the 2.6 Å cryo-EM map of ASCT2, a distinct density is evident in the proximity to the HP2 loop, to which we fitted the substrate glutamine (Supplementary Fig. 5a). The coordination pattern of glutamine in this structure resembles that observed in other ASCT2 structures[14,16] (Fig. 1d). Here, glutamine primarily interacts with conserved residues, specifically Asn471 and Asp464. The HP2 loop adopts a closed conformation, further stabilizing the bound glutamine. Additional non-protein densities are also evident in three positions near the glutamine density (Supplementary Fig. 5b–d). The locations of the three densities in ASCT2 align closely with equivalent Na^+ ion positions found in EAATs and archaeal transporters[10,19,40] (Supplementary Fig. 6a). In addition, the NMDG motif is in a compact conformation, and the coordination patterns of the densities in ASCT2 are similar to those observed for the Na^+ ions in concentrative transporters, indicating a strongly conserved Na^+-binding motif among all SLC1A family members (Supplementary Fig. 6b–d). Therefore, we interpret the three densities as Na^+ ions. At the Na1 site, the Na^+ ion is coordinated by the carboxyl group of Asp475 of TM8, along with the carbonyl groups of Gly382 and Asn386 (in the NMDG motif) of TM7 (Fig. 1e). The Na2 binding site is situated near the HP2b helix. The Na^+ ion interacts with the backbone carbonyl groups of Ser425, Val426, and Ala428 of HP2, as well as the sulfur side chain of Met387 in the NMDG motif of TM7 (Fig. 1f). The Na3 site is deeply embedded within the transport domain. The side chains of Asn386 and Asp388 in the NMDG motif of TM7 serve as coordinators for this Na^+ ion, along with the hydroxyl groups of Thr138 and Thr139 of TM3 and the backbone carbonyl oxygen of Phe135 of TM3 (Fig. 1g). Consequently, the densities provide structural evidence that the binding stoichiometry of one amino acid to 3 Na^+ ions is also conserved in exchangers. Another cryo-EM structure of ASCT2 published during the revision of this article supports our conclusion[44]. ASCT2 adopts the inward-facing conformation, revealing three Na^+ ions bound to the transport domain, which coincides well with the positions and coordination patterns of the Na^+ ions presented here.

ASCT2 resembles the Na^+-bound state when exposed to Na^+-deficient conditions

Since ASCT2 is an obligatory exchanger, we aimed to structurally investigate the number of Na^+ ions exchanged alongside the substrate. To explore this, we depleted ASCT2 of Na^+ ions and amino acid substrate and used cryo-EM to attempt to solve the structure of ASCT2 in the apo state in the presence of 200 mM KCl. We estimated that our sample preparation might contain maximally a few mM Na^+, a concentration that is well below the intracellular Na^+ concentration that ASCT2 would be exposed to under physiological conditions. For instance, in astrocytes[45], where ASCT2 is expressed, the intracellular concentration of Na^+ has been reported as 15–20 mM[46]. In addition, for structural studies of concentrative transporters, similar Na^+-depleted conditions were used[10,13,19,25]. In the latter case, the low Na^+ ion concentration was associated with the release of all three sodium ions and linked to the structural transition of the NMDG motif in TM7 from a compact to an extended conformation, which defines the apo conformation[10,13,19,25]. Our cryo-EM analysis yielded a C3-symmetrized reconstruction at 2.8Å resolution (Supplementary Fig. 7a–c). Initially, we anticipated the transporter to adopt a single conformation, assuming that the elevator transition would not be possible in the absence of substrate and Na^+ ions. Surprisingly, the cryo-EM map displayed a high level of flexibility in the transport domain. As presented in detail later, we employed symmetry expansion and 3D classification, unveiling two subpopulations of protomers (Supplementary Fig. 7c). One population contained outward-facing protomers that resemble the conformation found in the presence of glutamine and Na^+ ions. The other population represented the protomers sampling an intermediate outward state. For our analysis of the Na^+ and substrate coupling, we focus solely on the protomer in the outward-facing state, which was refined in local refinement to 2.9 Å resolution (Supplementary Fig. 7d). The conformational flexibility will be discussed in the last section.

In the outward-facing structure of ASCT2 in the absence of glutamine under Na^+-depleted conditions, the HP2 loop hinges away from the substrate binding site by approximately 4 Å compared to the substrate-bound structure (Gln-Na^+-$OFS^{HP2\text{-}cld}$), creating an aqueous pathway leading to the binding pocket (Fig. 2a). Notably, no density was identified in the substrate binding site, confirming that glutamine was not bound to the transport domain (Supplementary Fig. 8a). Based on these observations, we conclude that the structure obtained under Na^+-depleted conditions represents the outward-open substrate-free conformation of the transporter (referred further to as Na^+-depleted $OFS^{HP2\text{-}op}$ state). The positions of helical parts of HP2 showed minimal differences between the substrate-bound and substrate-free structures in the outward-facing state (Fig. 2b), but HP2b is longer in the conformation found under Na^+-depleted condition with residues Pro432-Val436 forming an additional turn of the helix. While in the substrate-bound state, the closed conformation of HP2 is stabilized by a hydrogen bond between Gln394 and Gly435, securing the occluded binding pocket, in the substrate-free state with open HP2, the nitrogen from the carbonyl group of Gln394 is flipped away, breaking the interaction with Gly435. Instead, a new hydrogen bond forms between Gln394 and Thr438, potentially stabilizing the HP2a helix near TM7. Notably, the loop connecting the two helical parts of HP2 (HP2a and HP2b) exhibited the least resolved cryo-EM density, indicative of increased dynamics of the gate compared to other parts of the protein.

Notwithstanding the differences in the gate region, the overall conformations of ASCT2 imaged with and without Na^+ ions are strikingly similar (with an overall r.m.s.d. of Cα atoms of 0.512 Å) (Fig. 2a). Surprisingly, the depletion of Na^+ ions did not lead to a structural change of the NMDG motif of TM7 into the extended state. Instead, the central part of TM7 retained its compact form, compatible with the binding of Na^+ ions (Fig. 2c). The residues involved in coordinating Na^+ ions at the Na1 and Na3 binding sites remain unchanged. Only the Na2 binding site was not fully formed due to the increased dynamics of HP2. Non-protein cryo-EM density was absent in the Na2 and Na3 sites, consistent with the notion that the ions had dissociated (Supplementary Fig. 8c, d). However, the Na1 site still displayed an excess density indicative of a bound Na^+ ion (Supplementary Fig. 8b). This observation contrasts sharply with structural studies of concentrative transporters, which had been similarly depleted of Na^+ ions and adopted a fully substrate-free state, characterized by an extended TM7 conformation[10,13,19,25] (Fig. 2d). In case of ASCT2, the TM7 failed to shift the conformation from a compact to an extended state when depleted from Na^+ ions. Hence, we hypothesize that ASCT2 favors the Na^+-like bound state even when exposed to low Na^+ concentration.

Previous studies have indicated that one Na^+ ion can bind to ASCT2 with high affinity (K_D in the μM range) in the absence of a transported amino acid substrate[47,48], which could explain the presence of the excess density at the Na1 site in our cryo-EM map. To investigate the possibility of the Na1 site as the high-affinity binding site, we computed the free energy profile for the Na^+ ion dissociation from the Na1 binding site in ASCT2 and Glt_{Tk}. We employed well-tempered metadynamics[49,50] using Glt_{Tk} and ASCT2 models that have TM7 in compact form and one Na^+ ion bound at the Na1 site. The space accessible to the ion was restricted to a cylindric volume around the Na1 binding site (Supplementary Fig. 9b). The free energy landscape for the Na^+ ion dissociation was defined by the number of contacts that the Na^+ ion establishes within the binding site (the sodium coordination number) and the distance to the border of the lipid bilayer (distance along the Z-axis). We observed two global minima (at a Z distance of 0–0.5 nm) in which the Na^+ ion explores the Na1 binding site (higher coordination number) and the Na3 site (lower

https://doi.org/10.1038/s41467-024-50888-8

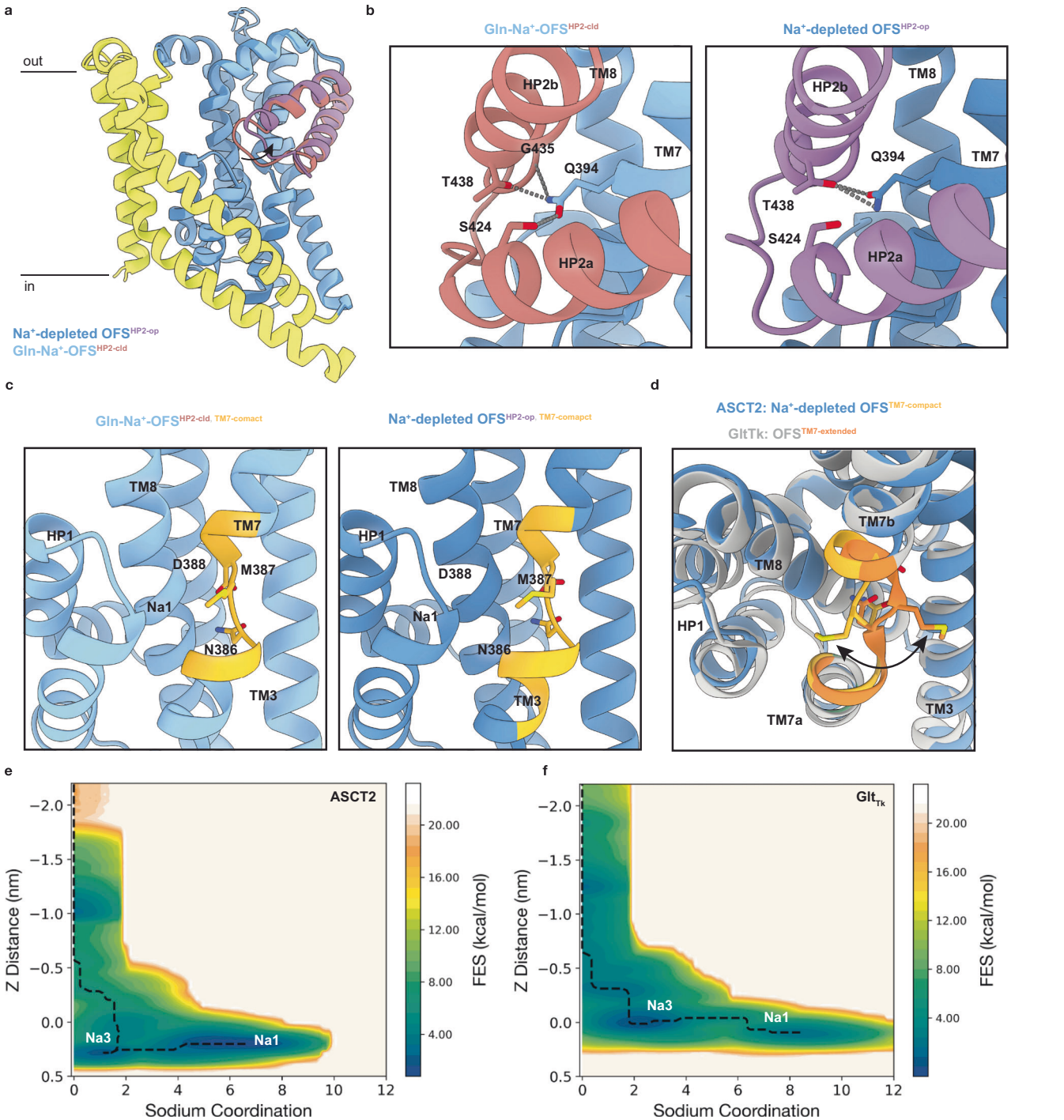

Fig. 2 | Structural comparison of ASCT2 in the presence of Na^+ ions and under Na^+-depleted conditions. a Superimposition of ASCT2 protomers imaged with the presence of glutamine and high Na^+ ion concentration (Gln-Na^+-OFS^{HP2cld}, transport domain in light blue and closed HP2 in salmon) and in the absence of substrate under the Na^+-depleted conditions (Na^+-depleted OFS^{HP2op}, transport domain in dark blue and open HP2 in purple). The scaffold domain in both structures is in yellow. **b** Comparison of interactions formed within the HP2a and HP2b in substrate-bound (left, transport domain in light blue and HP2 gate in salmon) and substrate-free (right, transport domain in dark blue and HP2 gate in purple) ASCT2. **c** Comparison of the conformation of the central region of TM7 in substrate-bound (left) and substrate-free (right) ASCT2. TM7 adopts the compact form (yellow) in substrate-bound ASCT2, forming the Na1 binding site (Na^+ ion shown in pink). In the substrate-free ASCT2, TM7 is still in the compact form (yellow) that facilitates the binding of a Na^+ ion at the Na1 binding site. Residues from the conserved NMDG motif are shown as sticks. **d** Superimposition of ASCT2 (dark blue) and Glt_{Tk} (gray, PDB 5WDY) structures solved under similar conditions with 200 mM KCl. Glt_{Tk} adopted the extended TM7 helix (orange), while ASCT2 still maintains the compact form of TM7 (yellow). Residues from the conserved NMDG motif are shown as sticks. **e**, **f** Free energy surface (FES) associated with the Na^+ ion binding in ASCT2 (**e**) and Glt_{Tk} (**f**) reweighted on the Z distance and the sodium number of contacts, showing a more tightly bound Na^+ ion at the Na1 in ASCT2 than in concentrative transporters such as Glt_{Tk}. The minimum energy path for the Na^+ ion dissociation is depicted as a black dashed line.

coordination number) (Fig. 2e, f). The Na^+ ion enters the water solution and dissociates from the transport domain at a Z distance of around −2 nm. The free energy barrier that the Na^+ ion must overcome to dissociate from the transport domain in ASCT2 is equal to 15.6 ± 0.3 kcal mol^{-1} (Fig. 2e, Supplementary Fig. 9c, e), while ΔG is lower for the concentrative transporter Glt_{Tk} (9.2 ± 0.3 kcal mol^{-1}) (Fig. 2f, Supplementary Fig. 9d, e). Hence, our free energy calculations support the conclusion that ASCT2 binds a Na^+ ion with high affinity at the Na1 binding site. Interestingly, the Na^+ binding sites in all members of the SLC1A family and archaeal homologs are structurally conserved, which prevents a straightforward structural explanation for the high-affinity Na^+ binding at the Na1 site.

TM7 does not unwind in exchangers

In concentrative transporters, the dissociation of Na^+ ions is linked to a rapid structural unwinding in TM7[51]. We wondered whether exchangers are also capable of this transition. We conducted unbiased MD simulations to explore the possibility of unwinding the TM7 in ASCT2 and used Glt_{Tk} as a control. Initially, we defined a reaction coordinate to describe the unwinding of TM7 in Glt_{Tk}, using the torsion angle of Cα atoms between Thr311-Met314-Asp315-Thr317 (Supplementary Fig. 10a, b). We carried out two separate 300 ns MD simulation runs of Glt_{Tk}, one with the transport domain adopting the compact TM7 conformation with bound Na^+ ions and substrate[19] (PDB ID 5E9S, Supplementary Fig. 10c), and the other with the extended TM7 conformation, as observed in the apo state in the absence of Na^+ ions and substrate[19] (PDB ID 5WDY, Supplementary Fig. 10f). For each case, we monitored the distribution of the torsional angle averaged over three protomers to characterize the TM7 conformation. The torsional angle oscillated around 180 degrees in Glt_{Tk} maintaining the compact TM7 conformation with bound Na^+ ions and substrate (Supplementary Fig. 10d, e). Conversely, in the absence of Na^+ ions and substrate, the torsional angle fluctuates around 100 degrees in Glt_{Tk} exhibiting the TM7 in the extended state (Supplementary Fig. 10g, h). Thus, this torsional angle allowed us to clearly distinguish between the two distinct TM7 conformations in concentrative transporters. Using the defined reaction coordinate, we investigated the structural transition of TM7 in Glt_{Tk}. Using the Glt_{Tk} structure adopting the compact TM7 conformation (PDB ID 5E9S) but with removed Na^+ ions and substrate, we conducted an MD simulation and observed a spontaneous transition of TM7 from the compact to extended conformation in 150 ns, as evidenced by two populations of the torsional angle distribution (Fig. 3a, b). The transition was clearly observed in two out of three protomers (Supplementary Fig. 10i). The variation among protomers is expected since we start from a non-equilibrium situation, and the change of TM7 state occurs at different times in each protomer. Upon the removal of Na^+ ions, the distribution of the torsional angle shifts from the initial oscillations around 180 degrees, via a minimum centered around the distribution of the torsional angle of 150 degrees, to the apo state with extended TM7, characterized by the distribution of the torsional angle around 100 degrees. The minimum centered around 150 degrees might not be significantly sampled when Na^+ ions are present in the binding sites. The transition was clearly observed in two out of three protomers (Supplementary Fig. 10i). We further performed an identical MD simulation run of ASCT2 exhibiting the compact form of TM7, also in the absence of substrate and Na^+ ions. We monitored the change in the torsional angle of equivalent Cα atoms Thr384-Met387-Asp388-Ala390 in ASCT2. In 300 ns of simulation, we observed that the torsional angle still oscillated around 190 degrees, indicating that TM7 remained compact despite the absence of ligands (Fig. 3c, d, Supplementary Fig. 10j). Unlike Glt_{Tk}, ASCT2 did not exhibit any spontaneous structural transition within the central region of TM7 upon substrate and Na^+ ion depletion. Besides, we observed a spontaneous binding of a Na^+ ion to the Na1 binding site within 100 ns in all three protomers of ASCT2 during the simulation run when the system included a low Na^+ concentration of 20 mM. In the case of the Glt_{Tk} simulation, such a Na^+ ion binding did not occur. A quantitative kinetic analysis of structural transition in TM7 and Na^+ ion binding would require averaging over several trajectories. Still, in this case, we found the results sufficient within the framework of a qualitative comparison between Glt_{Tk} and ASCT2, starting from the same initial structural conditions, providing a reasonable explanation for the observed differences. We thus conclude that the persisting compact state of TM7 retains a high-affinity Na^+ ion binding site at the Na1 site, stimulating the rapid rebinding of Na^+ ions to the transport domain in ASCT2.

Conformational transitions of the transport domain show an elevator movement in lipid nanodiscs

Despite the use of the belt protein 2N2, known to be able to form large nanodiscs of about 15–17 nm, the ASCT2 nanodisc particles showed a diameter of around 11 nm (Supplementary Fig. 11a). While many lipids surround the transport domain in both the upper and lower lipid leaflets, thereby filling the interface between the scaffold and transport domains (Supplementary Fig. 11b), in some places the belt protein tightly encloses the transporter. In doing so, it adapts to the triangular shape of the perimeter of the ASCT2 trimer, with the shortest distance between ASCT2 and the 2N2 protein around 3.5–3.8 Å, which may indicate a direct interaction between the transporter and the belt protein (Supplementary Fig. 11a). Remarkably, despite this potential interaction and the small size of the assembled nanodisc, both cryo-EM reconstructions of ASCT2 (in the presence of substrate and high Na^+ concentration, as well as without amino acid substrate and depleted of Na^+ ions) exhibited structural heterogeneity. We employed symmetry expansion and applied 3D classification to ASCT2 protomers to explore this variability. The dataset revealed several distinct conformations of protomers undergoing the elevator transition, thereby allowing to sample half of the transport cycle (Fig. 4, Supplementary Fig. 3c and 7c).

For substrate-bound ASCT2 protomers, three different global conformations of the transport domain were identified, which showed shifted relative positions to the scaffold domain (Fig. 4a, Supplementary Fig. 12a). Notably, the scaffold domain remained unchanged in all structures. The predominant conformation observed was the outward-facing state (Gln-Na^+-$OFS^{HP2\text{-}cld}$), which could be further classified based on subtle differences into three distinct subclasses, namely Gln-Na^+-$OFS.1^{HP2\text{-}cld}$, Gln-Na^+-$OFS.2^{HP2\text{-}cld}$, Gln-Na^+-$OFS.3^{HP2\text{-}cld}$ (Supplementary Fig. 12a). These classes were refined to a resolution of 2.7–2.8 Å (Supplementary Fig. 4b-d), revealing minor variations at the 1–2 angstrom level within the HP2 region (Supplementary Fig. 12b). The other two global conformations are referred to as Gln-Na^+-iOFS-$up^{HP2\text{-}cld}$ and Gln-Na^+-iOFS-$down^{HP2\text{-}cld}$, which both bear similarities to the previously observed intermediate outward-facing states in EAATs and archaeal homologs[13,21,52] (referred to as iOFS and iOFS* in previous studies). In the Gln-Na^+-iOFS-$down^{HP2\text{-}cld}$ state, the transport domain is further oriented to the inside than in the Gln-Na^+-iOFS-$up^{HP2\text{-}cld}$. The Gln-Na^+-iOFS-$up^{HP2\text{-}cld}$ and Gln-Na^+-iOFS-$down^{HP2\text{-}cld}$ were represented by 8% and 9% of particles and refined at 2.8 Å and 2.9 Å resolution, respectively (Supplementary Fig. 3c and 4e, f). During the transition from the Gln-Na^+-$OFS^{HP2\text{-}cld}$ to Gln-Na^+-iOFS-$up^{HP2\text{-}cld}$, the transport domain undergoes a rotation, resulting in a coordinated downward movement of HP2 by approximately 5 Å (Fig. 5a). During the transition from Gln-Na^+-iOFS-$up^{HP2\text{-}cld}$ to Gln-Na^+-iOFS-$down^{HP2\text{-}cld}$, the entire transport domain moves further inward, with all helices shifting down by 4 Å (Fig. 5b). HP2a and HP2b were pushed closer to the scaffold domain by about 5 Å in this state, and HP2a exhibited an increased helicity near the loop, likely contributing to the sealing of the substrate and sodium binding sites within the transport domain. The Gln-Na^+-iOFS-$down^{HP2\text{-}cld}$ conformation represents a midway point in the elevator mechanism, on its way to transition further to the intermediate inward-facing state depicted by the chloride-conducting conformation (ClCS) observed in Glt_{Ph}[26].

https://doi.org/10.1038/s41467-024-50888-8

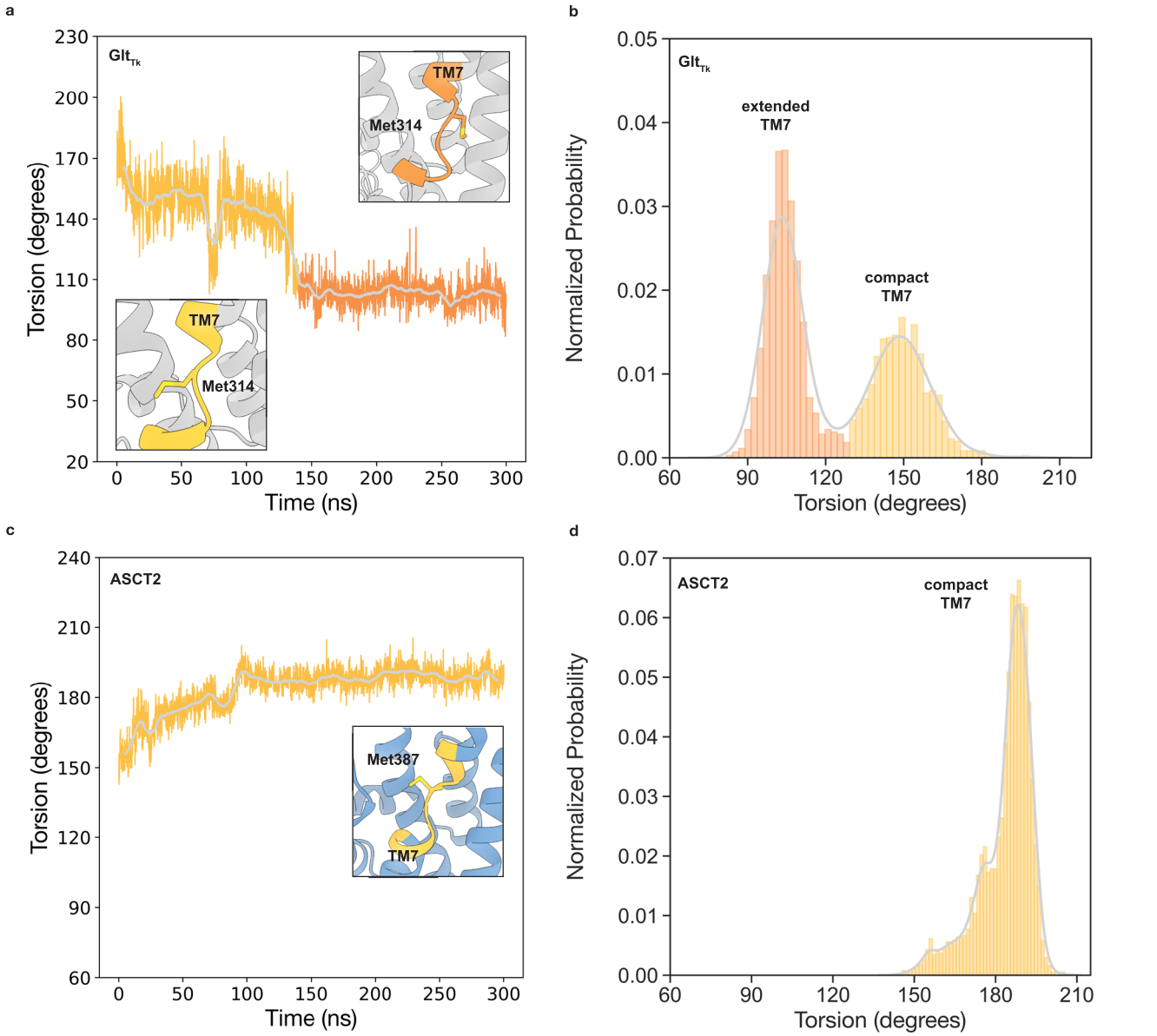

Fig. 3 | The structural transition of TM7. a The changes in torsional angle observed over the trajectory run in Glt$_{Tk}$. Close-ups represent the starting conformation, in which TM7 is in the compact form (yellow) found in substrate-bound states (lower left), and the final conformation with an extended TM7 (orange; upper right). **b** The distribution of torsional angle observed in the simulation of Glt$_{Tk}$ as seen in (**a**). **c**, The changes in torsional angle observed over the trajectory run in ASCT2. Close-up represents the starting conformation, in which TM7 is in the compact form (yellow), maintained throughout the entire simulation time (lower right). **d** The distribution of torsional angle observed in the simulation of ASCT2 as seen in (**c**).

Similarly, the dataset of substrate-free ASCT2 under Na^+-depleted conditions revealed conformational heterogeneity (Fig. 4b). Roughly 23% of the final particles define the protomer, adopting the outward-facing conformation described earlier (Na^+-depleted OFS$^{HP2\text{-}op}$). Remarkably, an almost equal number of particles (about 22%) contributed to a class that closely resembled the intermediate outward-facing state, featuring the transport domain in the up position (Na^+-depleted iOFS-up$^{HP2\text{-}op}$) at a resolution of 3.0 Å (Supplementary Fig. 7e). The conformational transition from OFS$^{HP2\text{-}op}$ to iOFS-up$^{HP2\text{-}op}$ state, in the absence of bound substrate, mirrored the transition seen when substrate was present, involving an overall rotation of the transport domain (Fig. 5c). The global conformation of the Gln-Na^+-iOFS-up$^{HP2\text{-}cld}$ and Na^+-depleted iOFS-up$^{HP2\text{-}op}$ protomers are very similar (RMSD of Cα atoms 0.430 Å) (Fig. 5d). However, a prominent difference was observed in the HP2 loop, which hinges away in the Na^+-depleted iOFS-up$^{HP2\text{-}op}$ state, thereby exposing the substrate binding site to the surrounding solvent. Furthermore, the positions of the HP2 helices differed between the two structures. In the Gln-Na^+-iOFS-up$^{HP2\text{-}cld}$ state, HP2a and HP2b are shifted towards the scaffold domain compared to the Na^+-depleted iOFS-up$^{HP2\text{-}op}$ state. It suggests that substrate binding and the subsequent closure of the HP2 loop primes for additional conformational rearrangements towards the iOFS-down state, which is only observed when the substrate is bound. Consequently, we speculate that the substrate-free carrier with an open HP2 loop cannot transition from the iOFS-up to the iOFS-down state. Therefore, the iOFS-up conformation appears to function as a checkpoint that enables glutamate transporters to distinguish between the substrate-bound and substrate-free transport domains.

Discussion

The cryo-EM structure of substrate-bound ASCT2 presented here reveals three Na^+ ions bound to the transport domain at the same

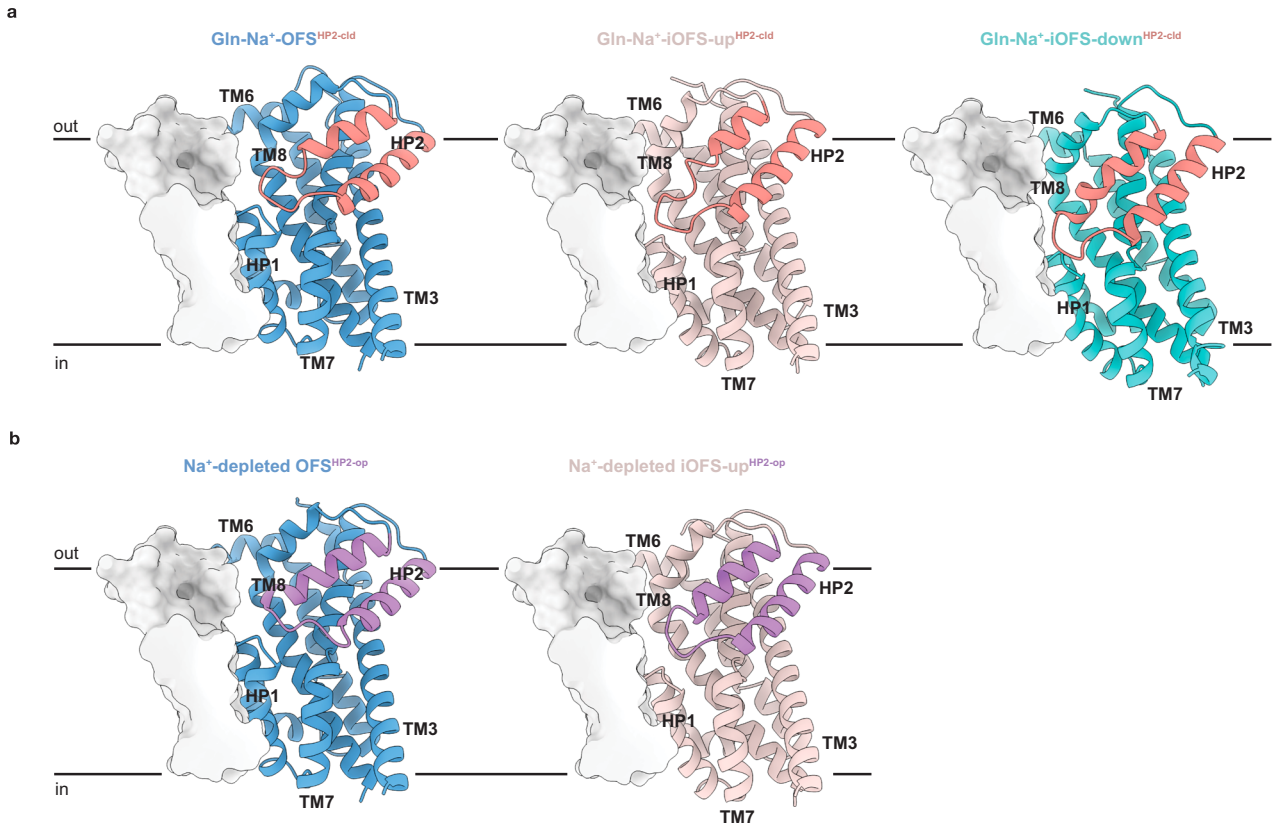

Fig. 4 | Conformational plasticity of ASCT2 protomers in lipid nanodiscs identified under substrate-bound and substrate-free conditions. a Structures of substrate-bound ASCT2 at three distinct conformational states: Gln-Na^+-OFS^{HP2cld} (blue), Gln-Na^+-iOFS-up^{HP2cld} (light pink), and Gln-Na^+-iOFS-$down^{HP2cld}$ (teal). **b** Structures of substrate-free ASCT2 at two distinct conformational states: Na^+-depleted OFS^{HP2op} (blue) and Na^+-depleted iOFS-up^{HP2op} (light pink). Each protomer is shown as a cartoon representation of the transport domain displayed in unique colors, and a surface colored in gray represents the scaffold domain. The scaffold domain acts as a reference point for the position of the transport domain in the membrane. The HP2 is displayed in salmon (closed conformation as seen in **a**) or purple (open conformation as seen in **b**).

conserved locations where sodium ions bind in the related concentrative transporters of the SLC1A family (Fig. 1). Hence, we conclude that the exchanger exhibits a conserved SLC1A binding stoichiometry of 1:3 (substrate to Na^+ ions). Surprisingly, under a Na^+- and substrate-depleted condition, the overall conformation of ASCT2 still resembled that of the Na^+-bound state, revealing two key structural features. Firstly, in our apparent 'apo' structure, the central region of TM7 remains in the compact form (Fig. 2a–d). MD simulations indicate that the transition in the TM7 region from a compact to an extended state does not occur in exchangers in the absence of bound Na^+ ions. This stands in strong contrast to concentrative transporters that swiftly adopt the apo conformation with an extended state of TM7[10,13,19,21,25] (Fig. 3). Secondly, an excess cryo-EM density at the Na1 binding site suggests that one Na^+ is still bound to the transporter, at least at Na^+ concentrations that are below those physiologically relevant. This supports previous experiments, which reported that one Na^+ ion remains constitutively bound to the transport domain with high affinity (in the μM range)[47]. Moreover, the rearrangement of residues forming the Na3 binding site bears the possibility that a Na^+ ion might also be bound at the Na3 site. Yet, we do not observe any density at the Na3 binding site (Supplementary Fig. 8d). Previous studies proposed two pathways for the Na^+ binding to the transport domain, among them one that includes an open HP2 gate forming a pathway for the Na^+ ion binding to the Na3 site[53]. An alternative pathway suggests that a Na^+ ion at the Na1 site can transition to the Na3 site while another Na^+ ion fills the Na1 site[54]. However, the free energy landscape showed that the Na1 site holds a higher affinity than the Na3 site, suggesting that one Na^+ ion would initially occupy the Na1 site. The free energy calculations confirm that the Na^+ ion bound at the Na1 site in ASCT2 requires a higher energy barrier for dissociation from the transport domain than the equivalent ion in concentrative transporter Glt_{Tk} (Fig. 2e, f). Hence, while the unbinding of the last Na^+ ion might occur occasionally, under physiological conditions, it would only happen at an extremely slow rate. This might also explain previous experiments that showed a coupling stoichiometry of substrate to Na^+ ions of 1:2 in ASCT2[33,34], implying that ASCT2 facilitates the exchange of one amino acid with two Na^+ ions, consistent with one Na^+ ion permanently bound to the transport domain. Therefore, the arrest of TM7 in its compact form and the associated occupied Na1 site – at physiological conditions presumably constitutively – hinder a closure of the HP2 and subsequent movement of the transport domain without substrate binding, thereby effectively locking it in an exchange mode.

Strikingly, the coordination patterns of Na^+ ions in ASCT2 and concentrative transporters are virtually identical. Neither the cryo-EM structures nor the MD trajectories point to obvious structural differences between exchangers and concentrators that could explain the differences in conformational changes of the TM7 region and the higher affinity of the Na1 site. The two observed features of ASCT2 are connected and might reinforce the function of ASCT2 as an exchanger. The compact TM7 facilitates the binding of Na^+ ions to the transport domain. Since the TM7 preferably retains the compact form, it supports the binding of Na^+ ions to ASCT2 at both intra- and extracellular sides where low and high concentrations of Na^+ ions are present,

https://doi.org/10.1038/s41467-024-50888-8

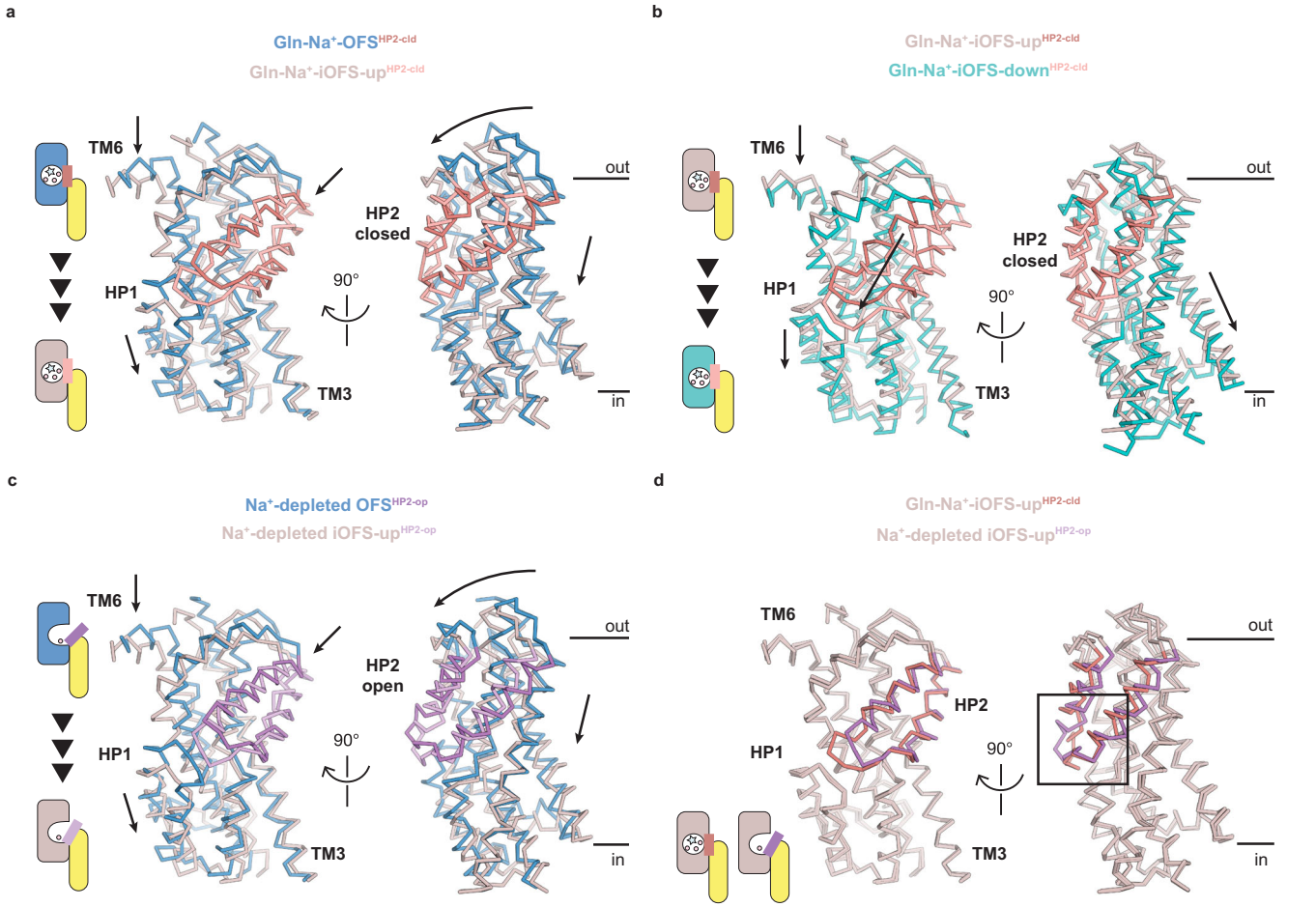

Fig. 5 | Comparison of conformational states of ASCT2 in lipid nanodiscs. **a** Conformational changes observed in the elevator transition from the Gln-Na^+-OFS (blue) to the Gln-Na^+-iOFS-up (light pink) states in substrate-bound ASCT2 with a closed HP2. **b** Conformational changes observed in the elevator transition from the Gln-Na^+-iOFS-up (light pink) to the Gln-Na^+-iOFS-down (teal) states in ASCT2 with a closed HP2. **c** Structural transition observed in substrate-free ASCT2 under Na^+-depleted conditions from the Na^+-depleted OFS (blue) state to the Na^+-depleted iOFS-up (light pink), featuring an open HP2 gate. **d** Superimposition of two iOFS-up (light pink) states in substrate-bound and substrate-free ASCT2, displaying structural differences in the HP2 region (closed in salmon and open in purple). The structures in all panels were superimposed based on atoms of scaffold domains; however, the scaffold domains were hidden for a clear representation of conformational differences.

respectively. Conversely, the tight binding of Na^+ ions also contributes to maintaining the TM7 in the compact state.

While the residues that are primarily responsible for the exchange mechanism observed in ASCTs remain elusive, recent cryo-EM structures of EAAT3[13] revealed how the conformation and dynamics of the HP2a and HP2b helices change and allow for adopting distinct conformations compatible with transmembrane movement in the substrate- or K^+-bound states. The conformational changes of HP2 are directly linked to the coordinated movement of residues within the NMDG motif of TM7 and the YE/DDR motifs of TM7b and TM8 involved in substrate and cation binding (Supplementary Fig. 13a). These residues form a complex, interdependent interaction network that changes upon binding and unbinding of cations and substrate. Past studies have shown that a single mutation of selected residues in the YE/DDR motif caused the change of the transport mode from accumulation to exchange of acidic amino acids[55–58], suggesting that a break in the complex interaction network changes the phenotype. In ASCT2, the interaction network is incomplete due to the substitution of three residues (Supplementary Fig. 13b). The arginine of the DDR motif is replaced by cysteine, which changes the substrate specificity towards neutral amino acids in ASCT2. The R447C mutation in EAAT3 locked the transporter in the electroneutral exchange mode[55], but the opposite mutation C467R in ASCT2 did not influence the transport mode[15]. Similarly, in EAATs, the glutamate of the YE motif has been considered as a residue that defines the proton-dependency. The E373Q mutation in EAAT3 impaired the net transport of glutamate yet supports the exchange of glutamate. However, the equivalent mutation Q393E in ASCT2 generated only the pH-sensitive transporter but failed to switch the transport mode[59]. Finally, a single mutation at the position of tyrosine in the YE motif in EAAT1 to phenylalanine (Y403F)[57] locks the transporter in the exchange mode but also causes an increase in sodium affinity. Although this residue does not directly coordinate any Na^+ ions, it might contribute to the synergistic interplay of residues in the transport domain and shift the preference to adopt the conformation with the compact TM7. We speculate that no single switch in ASCT2 can restore the network of interactions needed for a concentrator, while single mutations in concentrative transporters can break the network so that they become exchangers.

In the past, we determined the cryo-EM structure of the inward-facing conformation of ASCT2 in a detergent solution. In contrast, the structural analysis carried out in this study with ASCT2 reconstituted in a lipid bilayer-like nanodisc environment and analogous conditions, as used before, revealed primarily the outward-facing conformation. Careful re-analysis of the cryo-EM data of the inward-facing structure in detergent solution revealed no conformational flexibility with ASCT2 exclusively residing in a single state. In contrast, the nanodisc sample

exhibited significant conformational variability, with several outward-facing states sampling half of the elevator-like transport cycle but without reaching the inward-facing state (Fig. 4). Studies of Glt_{Tk} under analogous conditions also adopted lipid nanodisc sizes of 10–11 nm in diameter with a high degree of conformational heterogeneity encompassing almost the entire transport cycle[21]. Thus, we conclude that while the nanodiscs might be restricting ASCT2 from reaching an inward-facing state, it is unlikely that the observed states are artifacts but rather provide mechanistic relevant insights into the conformational plasticity in ASCT2. The conformational changes observed here might serve as checkpoints. The local sub-angstrom structural adjustments in the outward-facing state observed for the substrate-bound ASCT2 (Gln-Na^+-$OFS^{HP2\text{-}cld}$) might be necessary to probe a state compatible with the elevator transition into the first intermediate state in the up position (Gln-Na^+-iOFS-$up^{HP2\text{-}cld}$; Fig. 5a). The iOFS-up state is conserved in the archaeal homologs and the mammalian EAATs[13,21,25,52]. Under these saturating conditions, ASCT2 also visits another intermediate state in which the transport domain has moved slightly further down towards the inward-facing state (Gln-Na^+-iOFS-$down^{HP2\text{-}cld}$, Fig. 5b), which was also seen in cryo-EM studies of EAAT3[13] in the glutamate-bound state. ASCT2 in lipid nanodiscs in the absence of substrate can also reside in the intermediate state in the up position (iOFS-$up^{HP2\text{-}op}$, Fig. 5c). However, we could not identify any class among substrate-free protomers that resembles the intermediate state in the down position. Hence, the conserved iOFS-up conformation appears mechanistically critical for all members of the SLC1A family and may serve as a structural checkpoint in distinguishing between the translocation-competent and incompetent states (Fig. 5d). A prominent difference between exchangers and concentrative transporters is the position of the HP2 gate in the iOFS-up. ASCT2 features an open HP2 gate in the intermediate state, while EAATs assume a closed hairpin with an enlarged loop[13]. The difference might arise from the more complex transport cycle in EAATs that have to adopt conformation compatible with either Na^+ and amino acid or K^+ transport, while ASCTs mediate the exchange of amino acid and Na^+ ions.

In summary, we reveal the structural differences between concentrators and exchangers (Fig. 6). Under Na^+-depleted conditions, the TM7 in concentrative transporters transitions into an extended form, which is compatible with a closure of the HP2 gate and facilitates transmembrane movements of a substrate devoided transport domain across the membrane. Conversely, high Na^+ ion concentrations stabilize the open HP2 gate in concentrative transporters by conformational selection of a state with the central region of TM7 in a compact form. When only Na^+ ions are bound to the transport domain, the HP2 gate cannot close, ensuring a strict coupling to amino acid uptake. The HP2 can close only when the substrate and the third Na^+ ion bind, initiating the translocation of the substrate. In contrast, exchangers employ a stringent coupling mechanism. Exchangers constantly maintain TM7 in the compact conformation, even at low Na^+ ion concentrations, thus enhancing the high-affinity binding of one Na^+ ion to the transport domain. Under these conditions, the HP2 gate remains open, and only the binding of the amino acid substrate, along with two additional Na^+ ions, prompts the closure of HP2. Once HP2 has closed, the transmembrane movement of the transport domain can take place, effectively allowing only the shuffling of amino acids from one lipid leaflet to the other.

Methods

ASCT2 expression and purification

The full-length human ASCT2 protein was expressed and purified following the established protocol[14] with a few modifications. Briefly, ASCT2 was expressed in *Pichia pastoris* X-33 strain (Invitrogen) using either a fermenter or baffled flasks. Before the preparation of membrane vesicles, cells were diluted in buffer A (50 mM Tris-HCl, pH 7.4, 150 mM NaCl) supplemented with 3 mM $MgCl_2$, 0.1 mg ml^{-1} DNase A (Sigma-Aldrich) and 1 mM PMSF. Cells were lysed using a high-pressure cell lyser Maximator HPL6 at 40 kPsi and 4 °C by passing the cells four times. Subsequently, cell debris was removed by centrifugation at 12,074 × *g* for 30 min. The membrane vesicles were collected by ultracentrifugation for 120 min at 193,727 × *g* and 4 °C, resuspended in buffer B (25 mM Tris-HCl, pH 7.4, 300 mM NaCl, 10% glycerol), flash-frozen in liquid nitrogen, and stored at −80 °C for further use. ASCT2 was purified from an aliquot of membrane vesicles by solubilization in buffer B supplemented with 1 mM L-glutamine, 1% DDM, and 0.2% CHS for 1 h at 4 °C. The insoluble membrane fraction was removed by ultracentrifugation at 442,907 × *g* for 30 min. In the meantime, the Ni^{2+}-Sepharose resin was equilibrated with buffer C (20 mM Tris-HCl, pH 7.4, 300 mM NaCl, 10% glycerol, 1 mM glutamine). The supernatant containing soluble ASCT2 was supplemented with 50 mM imidazole, pH 7.4, and incubated with Ni^{2+}-Sepharose resin for 1 h at 4 °C. Afterward, unbound proteins were collected in flow-through using a disposable column, and the resin was washed with 20 column volumes (CV) of buffer C containing 0.05% DDM and 0.01% CHS. ASCT2 was eluted with buffer D (25 mM Tris-HCl, pH 7.4, 300 mM NaCl, 10% glycerol, 500 mM imidazole, pH 7.4, 1 mM L-glutamine) supplemented with 0.05% DDM and 0.01% CHS and purified with size-exclusion chromatography by application the sample onto a Superdex 200 10/300 gel filtration column (GE Healthcare) preequilibrated with buffer E (20 mM Tris-HCl, pH 7.4, 300 mM NaCl, 1 mM glutamine, 0.05% DDM, 0.01% CHS). The peak fractions were collected and used for further experiments.

ASCT2 reconstitution into liposomes and transport assay

Freshly purified ASCT2 was used for reconstitution into liposomes as previously described[14] with minor changes. During the reconstitution, one aliquot of *E. coli* polar lipids and egg PC at a ratio of 3:1 (w/w) and additionally 10% (w/w) cholesterol (Avanti Polar Lipids) was diluted to 4 mg ml^{-1} and destabilized with 10% Triton X-100. Subsequently, lipids were mixed with ASCT2 at a lipid-to-protein ratio of 250:1 (w/w). The assembly was supplemented with 1 mM glutamine to maintain the stability of ASCT2. The reconstitution mixture was incubated for 30 min at room temperature (RT), and aliquots of Biobeads were added in four steps: 25 mg ml^{-1} for 30 min at RT, 15 mg ml^{-1} for 1 h at 4 °C, 19 mg ml^{-1} with overnight incubation at 4 °C, and 29 mg ml^{-1} for 2 h on the next morning at 4 °C. The proteoliposomes were collected by centrifugation (30 min, 442,904 × *g*, 4 °C). To ensure the removal of traces of glutamine and NaCl, the proteoliposomes were washed with buffer F (20 mM Tris-HCl, pH 7.0) and centrifuged again (30 min, 442,904 × *g*, 4 °C). Further, the liposomes were resuspended in a small volume of buffer F, subjected to three freeze-thaw cycles, extruded 11 times through a 400 nm polycarbonate filter (Avestin), and collected by centrifugation (30 min, 442,904 × *g*, 4 °C). Finally, proteoliposomes were resuspended in buffer F, aliquoted, flash-frozen in liquid nitrogen, and stored in liquid nitrogen. For transport assay, an aliquot of proteoliposomes and empty liposomes was loaded with 10 mM glutamine and 50 mM NaCl or KCl by three freeze-thaw cycles. Next, the samples were extruded 11 times through a 400 nm polycarbonate filter (Avestin) and ultracentrifuged for 30 min at 4 °C and 442,904 × *g*. Finally, proteoliposomes were resuspended in a minimal volume of buffer F. The transport assay was carried out in a water bath at 25 °C with constant stirring. The external solution contained 5 μM unlabeled glutamine, 50 μM [^{3}H]-glutamine, and 50 mM NaCl or KCl. The amino acid exchange was initiated by the dilution of proteoliposomes in the external solution. The reaction was stopped at indicated time points by diluting an aliquot of solution with proteoliposomes in 2 ml of cold buffer F and filtering over a 0.45 μm filter (Portran BA-85, Whatman). The filter was washed additionally with 2 ml of cold buffer F. The radioactivity accumulated inside the proteoliposomes as a result of amino acid exchange was counted using a PerkinElmer Tri-Carb 2800RT liquid scintillation counter after dissolving the filter in 2 ml of scintillation liquid (Emulsifier Scintillator Plus, PerkinElmer).

https://doi.org/10.1038/s41467-024-50888-8

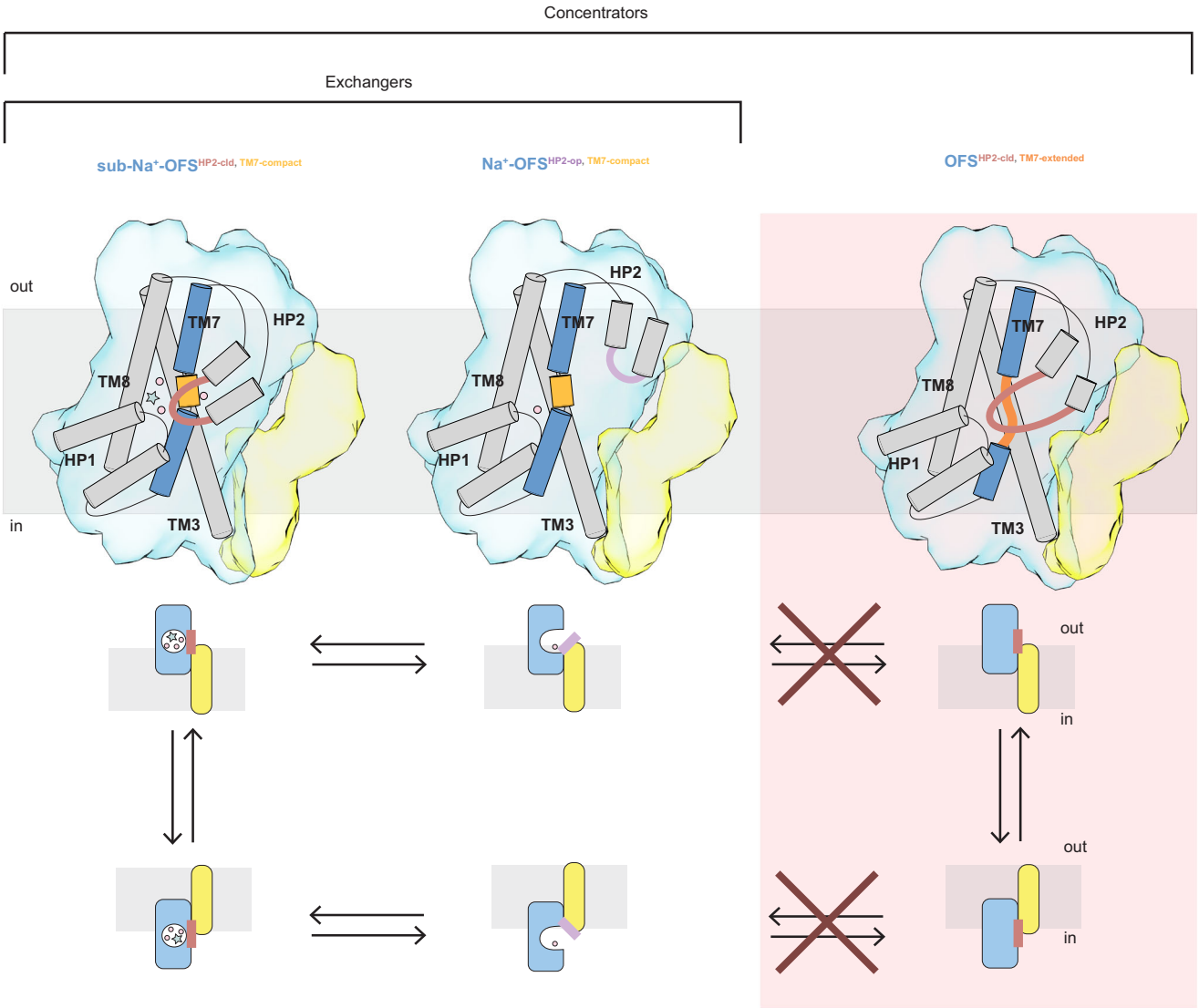

Fig. 6 | A scheme of the transport cycle and structural differences in concentrators and exchangers from the SLC1A family. The upper part depicts outward-facing protomers displaying the structural rearrangements of HP2 and TM7 at various stages of the transport cycle, with the respective schematic representation of protomers below. Considering the reversible nature of secondary transporters and the structural equivalence of the binding sites in the outward- and inward-facing states, the structural transitions apply to both outward- and inward-facing conformations. The transport and scaffold domains are visualized in blue and yellow, respectively, with displayed HP2 gate (closed in salmon and open in purple) and TM7 (compact in dark yellow and extended in orange). The membrane boundaries are shown as gray shadows. The part of the transport cycle restricted in exchangers is indicated by a red box, and crossed arrows signal the transition to the conformation that exchangers do not sample. In contrast to concentrators, upon substrate release, ASCT2 retains a bound Na^+ ion with a rigid TM7 in a compact state, prohibiting closure of the HP2 gate and a reorientation to the apo state, thereby effectively confining ASCT2 to an exchange mode.

ASCT2 reconstitution into lipid nanodiscs

The 2N2 membrane scaffold protein (MSP) was used for lipid nanodisc reconstitutions. The MSP2N2 protein was expressed and purified according to the established protocols[60]. The in-house purified *E. coli* polar lipids and egg PC at a ratio of 3:1 (w/w) and additionally 10% (w/w) cholesterol (Avanti Polar Lipids) were solubilized with 30 mM DDM/CHS and used for all nanodisc reconstitutions. For screening of nanodisc ratio, ASCT2 was reconstituted at ASCT2 (as trimer) to MSP to lipids molar ratios of 1:5:X, where X was equal to 70, 250, 500, 750, 1000, 1500, 2000. Freshly purified ASCT2 was mixed with solubilized lipids and incubated for 30 min on ice. Next, 2N2 protein was added, and the reaction was incubated for another 30 min on ice. Afterward, detergent was removed by overnight incubation with Biobeads (200 mg of beads ml^{-1} of the reaction) while gently nutating. Further, ASCT2 reconstituted in nanodiscs was separated from empty nanodiscs by incubation with Ni^{2+}-Sepharose resin for 1 h at 4 °C. The resin was washed with 10 CV of buffer C, and the protein was eluted with buffer D. The sample was purified by size-exclusion chromatography using a Superose 6 column equilibrated in buffer G (20 mM Tris-HCl, pH 7.4, 200 mM NaCl, 1 mM glutamine). For nanodisc reconstitution for cryo-EM analysis, ASCT2 was reconstituted at ASCT2 (as trimer) to MSP to lipid molar ratio of 1:5:70, and the purification protocol was the same as for the screening of nanodisc ratio with minor changes in gel filtration buffer. For the sample in the presence of Na^+ and glutamine, the gel filtration buffer included 200 mM NaCl and 1 mM glutamine, while for the sample in Na^+ and substrate-free condition, the gel filtration buffer contained 200 mM KCl instead of NaCl. The purified ASCT2 in nanodiscs was concentrated to ~1.5–2 mg ml^{-1} using an Amicon Ultra-0.5 ml concentrator (Merck) with a 100 kDa filter cut-off.

Cryo-EM sample preparation and data collection

2.8 μl of the sample was applied on holey-carbon cryo-EM grids (Quantifoil, Au R1.2/1.3, 300 mesh) glow-discharged (Edwards Scancoat 6) prior to freezing at 5 mA for 30 s. Grids were blotted for 2–3 s in a Vitrobot Mark IV (Thermo Fisher) at 15 °C and 100% humidity, plunged frozen into a liquid ethane-propane mixture, and stored in liquid nitrogen. For the dataset in the presence of Na^+ and glutamine, cryo-EM data was collected on a 300-keV Titan Krios microscope at the Netherlands Centre for Electron Nanoscopy (NeCEN) equipped with a BioQuantum K3 (Gatan) and using a 20-eV energy slit and a 100 μm objective aperture. The movies were recorded with EPU 2.10 (Thermo Fisher) operating the K3 in super-resolution counting mode and additional binning by two at the nominal magnification of 105,000 (pixel size of 0.836 Å) and an applied defocus range between −0.9 and −2.0 μm. Two exposures per hole were recorded. Each image was collected during 2.43 s exposure, collecting 76 frames with a total dose of about 60 electrons per $Å^2$. The targets for data collection were selected based on the ice thickness calculated using an in-house written script[61], and the quality of collected data was monitored on the fly using WRAP software[62]. For dataset at low Na^+ ion concentration, cryo-EM data was collected on a 200-keV Talos Arctica microscope at the University of Groningen equipped with a BioQuantum K2 (Gatan) using a 20-eV energy slit and a 100 μm objective aperture. The movies were recorded with SerialEM with the camera operation in counting mode at the nominal magnification of 130,000 (pixel size of 1.022 Å) with applied defocus between −0.9 and −1.9 μm. Each hole was imaged in the center during 9 s exposure, collecting 60 frames with a total dose of about 51 electrons per $Å^2$. The targets for data collection were selected based on the ice thickness calculated using an in-house written script[61], and the quality of collected data was monitored on the fly using FOCUS software[63].

Image processing of ASCT2 in the presence of Na^+ and substrate

A total of 14,117 movies were recorded in two sessions. Data was preprocessed using FOCUS software[63]. Movies were subjected to motion correction and dose weighting of frames in MotionCor2[64], and the CTF parameters were estimated on the movie frames with ctffind4.1[65]. Images showing ice contamination or poor CTF estimation were discarded, resulting in 8,730 micrographs used for further processing. A total of 7,639,781 particles were picked with crYOLO 1.7.6[66,67] using the general model (version N63_c17_27052020) with anchors set to 160 and subsequently imported into RELION 3.1.0[68]. Particles were extracted with a box size of 240, downscaled to 1.672 Å/pix, and imported to cryoSPARC 3.3.2[69]. After two rounds of 2D classification, 2D classes displaying high-resolution features were selected, and 2,961,087 particles were imported back to RELION 3.1.0 using PyEM script[70]. Subsequently, three rounds of 3D classification into ten classes without imposing symmetry were performed to clean the particles. In the first round of 3D classification, an initial model generated from the same dataset during the early attempts of processing and low-pass filtered to 30 Å was used as a reference. Subsequent 3D classifications used the best class of the previous job low-pass filtered to 20 Å as a reference. Particles were re-extracted to a full box size of 240 and subjected to another 3D classification that yielded the best class containing 1,023,628 particles. Those were refined by 3D refinement with applied C3 symmetry to 2.95 Å resolution after masking. After two rounds of CTF refinement (beam-tilt estimation, per-particle defocus, and per-micrograph astigmatism), the resolution improved to 2.82 Å after masking. All particles were subjected to another 3D classification into ten classes with applied C3 symmetry, which resulted in 95% of particles being classified into one class. 980,802 particles were used for further processing and underwent two rounds of CTF refinement and one round of Bayesian polishing[71], followed by another round of CTF refinement and masked 3D refinement with imposed C3 symmetry, resulting in a final reconstruction at 2.57 Å resolution. The conformational heterogeneity between protomers was investigated by employing symmetry expansion and 3D classification without alignment with a soft mask covering a single protomer. 2,942,406 protomers were classified into ten classes with tau fudge 128 over 50 iterations and yielded five classes representing distinct structural variability. Each class was further refined in masked refinement that resulted in a final resolution between 2.7 and 2.9 Å. Resolution of all maps was estimated using 0.143 cut-off criteria (gold-standard FSC) in postprocessing applying a mask around the protein excluding the nanodisc. Variations of the local resolution were estimated with RELION.

Image processing of ASCT2 at low Na^+ concentration

Two datasets with 1933 and 2212 movies were initially processed separately. MotionCor2[64] and ctffind4.1[65] within FOCUS[63] were used for motion correction and CTF parameters estimation, respectively. Low-quality images showing ice contamination or poor CTF estimation were discarded, resulting in 1633 and 1900 images used for further processing. 1,482,893 and 1,773,196 particles were picked separately using crYOLO 1.7.6[66,67] and the general model (version N63_c17_27052020) with anchors set to 160 and subsequently imported into RELION 3.1.0[68]. Particles were extracted with a box size of 256, downscaled to 2.044 Å/pix, and imported to cryoSPARC 3.3.2[69]. The initial processing was carried out in cryoSPARC. After one round of 2D classification, 2D classes displaying high-resolution features were selected, and the initial models were reconstructed using ab initio reconstruction, followed by heterogeneous refinement with ten classes. The best class was subjected to homogeneous refinement. Particles were imported back to RELION 3.1.0 using PyEM script[70] and re-extracted to a full box size of 256. Particles from both datasets were joined at this point, yielding 517,326 particles, which were imported again to cryoSPARC and subjected to multiple rounds of heterogeneous, homogeneous, and non-uniform refinement. The resulting reconstruction contained 192,201 particles and with a resolution of 2.84 Å. Particles were imported back to RELION and subjected to a few rounds of CTF refinement and Bayesian polishing[71], which resulted in a C3-symmetrized map at 2.84 Å resolution. Although the resolution did not improve, we used this map to identify structural heterogeneity in protomers. The particles were symmetry expanded and subjected to 3D classification without alignment. 576, 603 protomers were classified into ten classes with tau fudge 128 over 25 iterations and yielded two classes that represented distinct conformations. Both classes were further refined in the local 3D refinement with an applied mask into a final resolution of 2.9–3.0 Å. The resolution of all maps was estimated using 0.143 cut-off criteria (gold-standard FSC) with a mask applied in postprocessing. Variations of the local resolution were estimated with RELION.

Model building and refinement

The final maps were auto-sharpened with PHENIX[72,73] and used for model refinement, analysis, and figure preparation. The structure of ASCT2 in detergent micelle (PDB 6MPB) was fitted into cryo-EM maps in UCSF Chimera[74]. The models were manually adjusted in COOT[75]. The models were subjected to iterative rounds of real-space refinement in Phenix[72,73] and rebuilding errors in ISOLDE[76]. Figures were prepared with UCSF ChimeraX[77] and Chimera[74]. All programs used for image processing and model refinement were accessed through SBGrid[78].

System setup MD simulations

The crystal structures of the archaeal homolog Glt_{Tk} in the substrate-free apo state (PDB 5DWY) and in the presence of aspartate and Na^+ ions (PDB 5E9S), and cryo-EM structure of ASCT2 determined under Na^+-depleted conditions (PDB 8QRV) were used as the starting configurations[19]. The protein models were embedded in 1-palmitoyl-2-oleoyl-sn-glycero-3-phosphocholine (POPC) lipid bilayer with 10%

cholesterol distributed in both upper and lower leaflets and solvated with water using the CHARMM-GUI web server[79] (Supplementary Fig. 9a). We performed two metadynamics simulations to calculate the free energy landscape of Na^+ ion binding and unbinding in Glt_{Tk} and ASCT2 and four unbiased molecular dynamics simulations using different initial system setups of Glt_{Tk} and ASCT2 to study the TM7 unwinding. Supplementary Table 3 represents a detailed summary of the system setups (PDB ID, TM7 state, the presence of substrate or Na^+ ions, and salt concentration in the system) for all conducted simulations. For metadynamics calculations, we used Glt_{Tk} (PDB 5E9S) and ASCT2 (PDB 8QRV) structures, which exhibit TM7 in the compact form and one Na^+ ion bound to the Na1 site. The systems included 100 mM NaCl. For the unbiased molecular dynamics simulations, we created three different setups:

1. Glt_{Tk} (PDB 5E9S) with the substrate and Na^+ ions bound to the binding sites and TM7 in the compact state (including 100 mM NaCl).
2. Glt_{Tk} (PDB 5DWY) in the apo state without the substrate and Na^+ ions in the binding sites and TM7 in the extended state (including 20 mM NaCl).
3. Glt_{Tk} (PDB 5E9S) without the substrate and Na^+ ions, but TM7 adopts the compact conformation (including 20 mM NaCl).

The simulation setup of ASCT2 (PDB 8QRV) for the unbiased simulation of TM7 unwinding represents the structure with TM7 in the compact form with neither the substrate nor Na^+ ions bound to the transporter. The ASCT2 system included 20 mM NaCl and KCl.

Because of the absence of pre-existing reaction coordinates to study the specific and localized movement of the conformational change in TM7, we selected the torsional angle defined between the Cα atoms Thr311-Met314-Asp315-Thr317 in Glt_{Tk} and the equivalent atoms Thr384-Met387-Asp388-Ala390 in ASCT2. The selected reaction coordinate uniquely distinguishes between the compact and extended states.

The simulation boxes contained ~150,000 atoms ($L_x = 100$ Å, $L_y = 100$ Å, and $L_z = 130$ Å). Protein, lipids, ions, and water were described with CHARMM36m[80,81] with the inclusion of CMAP and NBFIX terms, CHARMM36[82], and TIP3P[83] force fields, respectively. Long-range interactions were evaluated using particle-mesh Ewald summation[84] with a 12 Å cut-off in real space. Lennard–Jones (LJ) interactions were truncated at 12 Å with an atom-based force switching function, which starts to be effective at 10 Å. The integration time step was set at 2 fs. Bonds involving hydrogen atoms were constrained using the LINCS algorithm[85]. A Nosé–Hoover chain thermostat[86] was used to maintain the temperature at 300 K. A semi-isotropic Parrinello–Rahman barostat[87] with a reference pressure of 1 atm and isothermal compressibility of 4.5×10^{-5} bar^{-1} was used to maintain the pressure of the system. The equilibration of the systems includes sequential coupling with a thermostat (NVT) and barostat (NPT), along with the gradual reduction of position restraints on the protein and lipids. A detailed and schematic overview of all the equilibration steps is given in Supplementary Table 4. After energy minimization and equilibration, the systems were simulated for 300 ns. All simulations were performed using the GROMACS-2021 package[88].

Well-tempered metadynamics and free energy calculations

We employed well-tempered metadynamics (MTD) to construct the free energy landscapes for the sodium binding and unbinding to Glt_{Tk} and ASCT2[49,89–91]. We defined a cylindric volume spanning from the center of the protein, i.e., the coordination domain, to the solution, where the Na^+ ion is allowed to explore a confined volume around the binding region (Supplementary Fig. 9b)[50,92]. The collective variable (CV) is the distance between the Na^+ ion and the center of mass of a selected group of residues forming the Na1, Na2, and Na3 binding sites (Gly382, Asn386, Asn471, Asp475, Asp388, Thr138, Thr139, Met387, Ser425, Met387, Ala428, Thr384 in ASCT2 and the residues in equivalent positions in Glt_{Tk}), projected along the z-axis (Z distance). The center of mass coordinates for ASCT2 and Glt_{Tk} may differ, resulting in slight variations (few Å) in the positions of the sodium binding site along the projected Z-axis distance. The cylinder has a radius of 0.6 nm and a height of 2.7 nm (Supplementary Fig. 7b). The restriction of the Na^+ ion within the defined space is achieved by adding repulsive potential at the boundary of the cylinder. In particular, the restraint potential, with a harmonic constant equal to 150 kJ mol^{-1} $Å^{-2}$ (≈ 35.8 kcal mol^{-1} $Å^{-2}$), becomes effective when the CV is smaller than −2.2 nm or greater than 0.5 and when the cylinder radius is larger than 0.6 nm. The parameters to run the MTD are the same as used for the unbiased simulations with the addition of the following parameters for the deposited bias: Gaussian height 1.2 kJ mol^{-1} (≈0.29 kcal mol^{-1}), Gaussian sigma 1 Å, bias factor 20, and Gaussian deposition rate of 1 ps. The simulations were run for a time of 250 and 270 ns for ASCT2 and Glt_{Tk}, respectively, and the convergence was controlled by observing the behavior of the CV, the time evolution of the free energy profiles, and the difference in the free energy minimum and maximum values of the PMF over the simulation time. The errors for the free energies were evaluated using the block analysis, with a time interval of 4 ns, where they reached a plateau at 0.3 Kcal/mol. The free energy surfaces were obtained using the algorithm of Tiwary and Parrinello[93], reweighting on the CV (1D profiles, Supplementary Fig. 9c) or the CV and the Na^+ ion coordination number (2D profiles, Fig. 2e, f), defined as the number of contacts between the Na^+ ion and the group of residues of the Na1 binding site. As the coordination number was not utilized as CV, the quantitative free energy analysis was extrapolated from the one-dimensional profiles. The free energies are evaluated as the difference between the bound (the Na^+ ion bound in the binding pocket, corresponding to a value of the CV of 0–05 nm) and unbound state (the Na^+ ion in the solution, corresponding to a value of the CV of −2.0 nm). The WT-MTD simulations were performed using the GROMACS-2021 package[88] patched with the PLUMED 2.5 plugin[94,95]. During the MTD simulations, the Na^+ ion is restrained to remain inside a cylinder-shaped potential, which limits the free exploration of the solvent environment. This approach facilitates the movement of the ion, allowing it to sample several crossing events and speeding up the convergence. However, it is recognized that a loss of entropy affects the calculated free energies. The effect of the cylindrical restraint can be accounted for, and the missing entropic contribution has been estimated analytically for the funnel MTD, which uses the same cylindrical restraint[50,90]. The ion-protein binding free energy △G is calculated as follows:

$$\Delta G = \Delta G_{MET} - k_b T \ln\left(\pi R_{cyl}^2 C^0 \int dz \exp\left(\left(k_B T\right)^{-1}\left(W(z) - W_{ref}\right)\right)\right) \quad (1)$$

Where $\triangle G_{MET}$ is the free energy difference obtained by the metadynamics simulations, R is the radius of the cylinder, C^0 is the standard concentration of 1/1660 $Å^{-3}$, k_b is the Boltzmann constant, T is the system temperature, $W(z)$ is the potential of the mean force along the cylinder axis, and W_{ref} is its value in the unbound state.

The minimum energy path analysis on the 2D free energy landscape was conducted using the MEPSA 1.4 software[96], selecting the node-by-node modality for path generation.

Reporting summary

Further information on research design is available in the Nature Portfolio Reporting Summary linked to this article.

Data availability

The source data underlying Fig. 1a are provided as a Source Data file. The cryo-EM images generated in this study have been deposited in the Electron Microscopy Public Image Archive (EMPIAR)[97] under accession codes EMPIAR-11904 (ASCT2 in lipid nanodiscs with bound glutamine

and Na^+ ions) and EMPIAR-11905 (ASCT2 in lipid nanodiscs under Na^+-depleted conditions). The cryo-EM maps have been deposited in the Electron Microscopy Data Bank (EMDB) under accession codes EMD-18621 (ASCT2 trimer in MSP2N2 lipid nanodiscs with bound glutamine and Na^+ ions in the outward-facing state, Gln-Na^+-OFS$^{HP2\text{-}cld}$), EMD-18622 (ASCT2 protomer in MSP2N2 lipid nanodiscs with bound glutamine and Na^+ ions in Gln-Na^+-OFS.1$^{HP2\text{-}cld}$), EMD-18623 (ASCT2 protomer in MSP2N2 lipid nanodiscs with bound glutamine and Na^+ ions in Gln-Na^+-OFS.2$^{HP2\text{-}cld}$), EMD-18624 (ASCT2 protomer in MSP2N2 lipid nanodiscs with bound glutamine and Na^+ ions in Gln-Na^+-OFS.3$^{HP2\text{-}cld}$), EMD-18625 (ASCT2 protomer in MSP2N2 lipid nanodiscs with bound glutamine and Na^+ ions in the intermediate outward-facing state; Gln-Na^+-iOFS-up$^{HP2\text{-}cld}$), EMD-18626 (ASCT2 protomer in MSP2N2 lipid nanodiscs with bound glutamine and Na^+ ions in the intermediate outward-facing state; Gln-Na^+-iOFS-down$^{HP2\text{-}cld}$), EMD-18627 (ASCT2 protomer in MSP2N2 lipid nanodiscs under Na^+-depleted conditions in the outward-facing state; Na^+-depleted OFS$^{HP2\text{-}op}$), EMD-18628 (ASCT2 protomer in MSP2N2 lipid nanodiscs under Na^+-depleted conditions in the intermediate outward-facing state; Na^+-depleted iOFS-up$^{HP2\text{-}op}$). The atomic coordinated have been deposited in the Protein Data Bank (PDB) under accession codes 8QRO (ASCT2 trimer in MSP2N2 lipid nanodiscs with bound glutamine and Na^+ ions in the outward-facing state, Gln-Na^+-OFS$^{HP2\text{-}cld}$), 8QRP (ASCT2 protomer in MSP2N2 lipid nanodiscs with bound glutamine and Na^+ ions in Gln-Na^+-OFS.1$^{HP2\text{-}cld}$), 8QRQ (ASCT2 protomer in MSP2N2 lipid nanodiscs with bound glutamine and Na^+ ions in Gln-Na^+-OFS.2$^{HP2\text{-}cld}$), 8QRR (ASCT2 protomer in MSP2N2 lipid nanodiscs with bound glutamine and Na^+ ions in Gln-Na^+-OFS.3$^{HP2\text{-}cld}$), 8QRS (ASCT2 protomer in MSP2N2 lipid nanodiscs with bound glutamine and Na^+ ions in the intermediate outward-facing state; Gln-Na^+-iOFS-up$^{HP2\text{-}cld}$), 8QRU (ASCT2 protomer in MSP2N2 lipid nanodiscs with bound glutamine and Na^+ ions in the intermediate outward-facing state, Gln-Na^+-iOFS-down$^{HP2\text{-}cld}$), 8QRV (ASCT2 protomer in MSP2N2 lipid nanodiscs under Na^+-depleted conditions in the outward-facing state; Na^+-depleted OFS$^{HP2\text{-}op}$), 8QRW (ASCT2 protomer in MSP2N2 lipid nanodiscs under Na^+-depleted conditions in the intermediate outward-facing state; Na^+-depleted iOFS-up$^{HP2\text{-}op}$). The molecular dynamics data (PDB snapshots, cleaned trajectories, starting structure, simulation parameters) generated in this study have been deposited in the Zenodo repository under accession code 10613370. Source data are provided with this paper.

References

1. Bröer, S. & Bröer, A. Amino acid homeostasis and signalling in mammalian cells and organisms. *Biochem. J.* **474**, 1935–1963 (2017).
2. Chen, M. et al. Loss of RACK1 promotes glutamine addiction via activating AKT/mTOR/ASCT2 axis to facilitate tumor growth in gastric cancer. *Cell Oncol*. https://doi.org/10.1007/s13402-023-00854-1 (2023).
3. Ni, F. et al. Critical role of ASCT2-mediated amino acid metabolism in promoting leukaemia development and progression. *Nat. Metab.* **1**, 390–403 (2019).
4. Lin, J. et al. SLC1A5 silencing inhibits esophageal cancer growth via cell cycle arrest and apoptosis. *Cell. Physiol. Biochem.* **48**, 397 (2018).
5. Toda, K. et al. Clinical role of ASCT2 (SLC1A5) in KRAS-mutated colorectal cancer. *Int. J. Mol. Sci.* **18**, 1632 (2017).
6. Marshall, A. D. et al. ASCT2 regulates glutamine uptake and cell growth in endometrial carcinoma. *Oncogenesis* **6**, e367 (2017).
7. Kanai, Y. et al. The SLC1 high-affinity glutamate and neutral amino acid transporter family. *Mol. Asp. Med.* **34**, 108–120 (2013).
8. Canul-Tec, J. C. et al. Structure and allosteric inhibition of excitatory amino acid transporter 1. *Nature* **544**, 446–451 (2017).
9. Canul-Tec, J. C. et al. The ion-coupling mechanism of human excitatory amino acid transporters. *EMBO J.* **41**, 19 (2022).
10. Qiu, B., Matthies, D., Fortea, E., Yu, Z. & Boudker, O. Cryo-EM structures of excitatory amino acid transporter 3 visualize coupled substrate, sodium, and proton binding and transport. *Sci. Adv.* **7**, eabf5814 (2021).
11. Zhang, Z. et al. Structural basis of ligand binding modes of human EAAT2. *Nat. Commun.* **13**, 3329 (2022).
12. Kato, T. et al. Structural insights into inhibitory mechanism of human excitatory amino acid transporter EAAT2. *Nat. Commun.* **13**, 4714 (2022).
13. Qiu, B. & Boudker, O. Symport and antiport mechanisms of human glutamate transporters. *Nat. Commun.* **14**, 2579 (2023).
14. Garaeva, A. A. et al. Cryo-EM structure of the human neutral amino acid transporter ASCT2. *Nat. Struct. Mol. Biol.* **25**, 515–521 (2018).
15. Garaeva, A. A., Guskov, A., Slotboom, D. J. & Paulino, C. A one-gate elevator mechanism for the human neutral amino acid transporter ASCT2. *Nat. Commun.* **10**, 3427 (2019).
16. Yu, X. et al. Cryo-EM structures of the human glutamine transporter SLC1A5 (ASCT2) in the outward-facing conformation. *eLife* **8**, e48120 (2019).
17. Garibsingh, R. A. et al. Rational design of ASCT2 inhibitors using an integrated experimental-computational approach. *Proc. Natl Acad. Sci. USA* **118**, 10 (2021).
18. Stehantsev, P. et al. A structural view onto disease-linked mutations in the human neutral amino acid exchanger ASCT1. *Comput. Struct. Biotechnol. J.* **19**, 5246–5254 (2021).
19. Guskov, A., Jensen, S., Faustino, I., Marrink, S. J. & Slotboom, D. J. Coupled binding mechanism of three sodium ions and aspartate in the glutamate transporter homologue GltTk. *Nat. Commun.* **7**, 13420 (2016).
20. Arkhipova, V. et al. Binding and transport of D-aspartate by the glutamate transporter homolog GltTk. *eLife* **8**, e45286 (2019).
21. Arkhipova, V., Guskov, A. & Slotboom, D. J. Structural ensemble of a glutamate transporter homologue in lipid nanodisc environment. *Nat. Commun.* **11**, 998 (2020).
22. Yernool, D., Boudker, O., Jin, Y. & Gouaux, E. Structure of a glutamate transporter homologue from Pyrococcus horikoshii. *Nature* **431**, 811–818 (2004).
23. Boudker, O., Ryan, R. M., Yernool, D., Shimamoto, K. & Gouaux, E. Coupling substrate and ion binding to extracellular gate of a sodium-dependent aspartate transporter. *Nature* **445**, 387–393 (2007).
24. Reyes, N., Ginter, C. & Boudker, O. Transport mechanism of a bacterial homologue of glutamate transporters. *Nature* **462**, 880–885 (2009).
25. Wang, X. & Boudker, O. Large domain movements through the lipid bilayer mediate substrate release and inhibition of glutamate transporters. *eLife* **9**, e58417 (2020).
26. Chen, I. et al. Glutamate transporters have a chloride channel with two hydrophobic gates. *Nature* **591**, 327–331 (2021).
27. Slotboom, D. J., Konings, W. N. & Lolkema, J. S. Structural features of the glutamate transporter family. *Microbiol. Mol. Biol. R.* **63**, 293–29 (1999).
28. Grewer, C. et al. Individual subunits of the glutamate transporter EAAC1 homotrimer function independently of each other. *Biochemistry* **44**, 11913–11923 (2005).
29. Koch, H. P., Brown, R. L. & Larsson, H. P. The glutamate-activated anion conductance in excitatory amino acid transporters is gated independently by the individual subunits. *J. Neurosci.* **27**, 2943–2947 (2007).
30. Groeneveld, M. & Slotboom, D. J. Na(+):aspartate coupling stoichiometry in the glutamate transporter homologue Glt(Ph). *Biochemistry* **49**, 3511–3513 (2010).
31. Levy, L. M., Warr, O. & Attwell, D. Stoichiometry of the glial glutamate transporter GLT-1 expressed inducibly in a Chinese hamster ovary cell line selected for low endogenous Na+-dependent glutamate uptake. *J. Neurosci.* **18**, 9620–9628 (1998).

32. Owe, S. G., Marcaggi, P. & Attwell, D. The ionic stoichiometry of the GLAST glutamate transporter in salamander retinal glia. *J. Physiol.* **577**, 591–599 (2006).
33. Mazza, T., Scalise, M., Pappacoda, G., Pochini, L. & Indiveri, C. The involvement of sodium in the function of the human amino acid transporter ASCT2. *FEBS Lett.* **595**, 3030–3041 (2021).
34. Wang, J., Dong, Y. & Grewer, C. Functional and kinetic comparison of alanine cysteine serine transporters ASCT1 and ASCT2. *Biomolecules* **12**, 113 (2022).
35. Huang, Z. & Tajkhorshid, E. Dynamics of the extracellular gate and ion-substrate coupling in the glutamate transporter. *Biophys. J.* **95**, 2292–2300 (2008).
36. Shrivastava, I. H., Jiang, J., Amara, S. G. & Bahar, I. Time-resolved mechanism of extracellular gate opening and substrate binding in a glutamate transporter. *J. Biol. Chem.* **283**, 28680–28690 (2008).
37. Huang, Z. & Tajkhorshid, E. Identification of the third Na+ site and the sequence of extracellular binding events in the glutamate transporter. *Biophys. J.* **99**, 1416–1425 (2010).
38. Bastug, T. et al. Position of the third Na+ site in the aspartate transporter GltPh and the human glutamate transporter, EAAT1. *PLoS ONE* **7**, e33058 (2012).
39. Focke, P. J., Moenne-Loccoz, P. & Larsson, H. P. Opposite movement of the external gate of a glutamate transporter homolog upon binding cotransported sodium compared with substrate. *J. Neurosci.* **31**, 6255–6262 (2011).
40. Verdon, G., Oh, S., Serio, R. N. & Boudker, O. Coupled ion binding and structural transitions along the transport cycle of glutamate transporters. *eLife* **3**, e02283 (2014).
41. Oh, S. & Boudker, O. Kinetic mechanism of coupled binding in sodium-aspartate symporter GltPh. *Elife* **7**, e37291 (2018).
42. Amorino, G. P. & Fox, M. H. Intracellular Na^+ measurements using sodium green tetraacetate with flow cytometry. *Cytometry* **21**, 248–256 (1995).
43. Broer, A., Wagner, C., Lang, F. & Broer, S. Neutral amino acid transporter ASCT2 displays substrate-induced Na+ exchange and a substrate-gated anion conductance. *Biochem. J.* **346 Pt 3**, 705–710 (2000).
44. Khare, S. et al. Receptor-recognition and antiviral mechanisms of retrovirus-derived human proteins. *Nat. Struct. Mol. Biol.* https://doi.org/10.1038/s41594-024-01295-6 (2024).
45. Broer, A. et al. The astroglial ASCT2 amino acid transporter as a mediator of glutamine efflux. *J. Neurochem.* **73**, 2184–2194 (1999).
46. Verkhratsky, A. & Nedergaard, M. Physiology of astroglia. *Physiol. Rev.* **98**, 239–389 (2018).
47. Zander, C. B., Albers, T. & Grewer, C. Voltage-dependent processes in the electroneutral amino acid exchanger ASCT2. *J. Gen. Physiol.* **141**, 659–672 (2013).
48. Tao, Z., Zhang, Z. & Grewer, C. Neutralization of the aspartic acid residue Asp-367, but not Asp-454, inhibits binding of Na+ to the glutamate-free form and cycling of the glutamate transporter EAAC1. *J. Biol. Chem.* **281**, 10263–10272 (2006).
49. Barducci, A., Bussi, G., Parrinello, M. & Well-Tempered Metadynamics: a smoothly converging and tunable free-energy method. *Phys. Rev. Lett.* **100**, 020603 (2008).
50. Limongelli, V., Bonomi, M. & Parrinello, M. Funnel metadynamics as accurate binding free-energy method. *Proc. Natl Acad. Sci. USA* **110**, 6358–6363 (2013).
51. Zhou, W., Trinco, G., Slotboom, D. J., Forrest, L. R. & Faraldo-Gómez, J. D. On the role of a conserved methionine in the Na+-coupling mechanism of a neurotransmitter transporter homolog. *Neurochem. Res.* **47**, 163–175 (2022).
52. Verdon, G. & Boudker, O. Crystal structure of an asymmetric trimer of a bacterial glutamate transporter homolog. *Nat. Struct. Mol. Biol.* **19**, 355–357 (2012).
53. Riederer, E. A., Moënne-Loccoz, P. & Valiyaveetil, F. I. Distinct roles of the Na^+ binding sites in the allosteric coupling mechanism of the glutamate transporter homolog, Glt_{Ph}. *Proc. Natl Acad. Sci. USA* **119**, e2121653119 (2022).
54. Alleva, C. et al. Na^+-dependent gate dynamics and electrostatic attraction ensure substrate coupling in glutamate transporters. *Sci. Adv.* **6**, eaba9854 (2020).
55. Bendahan, A. et al. Arginine 447 plays a pivotal role in substrate interactions in a neuronal glutamate transporter. *J. Biol. Chem.* **275**, 37436–37442 (2000).
56. Kavanaugh, M. P., Bendahan, A., Zerangue, N., Zhang, Y. & Kanner, B. I. Mutation of an amino acid residue influencing potassium coupling in the glutamate transporter GLT-1 induces obligate exchange. *J. Biol. Chem.* **272**, 1703–1708 (1997).
57. Zhang, Y., Bendahan, A., Zarbiv, R., Kavanaugh, M. P. & Kanner, B. I. Molecular determinant of ion selectivity of a (Na^+ + K^+)-coupled rat brain glutamate transporter. *Proc. Natl Acad. Sci. USA* **95**, 751–755 (1998).
58. Rosental, N., Gameiro, A., Grewer, C. & Kanner, B. I. A conserved aspartate residue located at the extracellular end of the binding pocket controls cation interactions in brain glutamate transporters. *J. Biol. Chem.* **286**, 41381–41390 (2011).
59. Grewer, C., Watzke, N., Rauen, T. & Bicho, A. Is the glutamate residue Glu-373 the proton acceptor of the excitatory amino acid carrier 1? *J. Biol. Chem.* **278**, 2585–2592 (2003).
60. Ritchie, T. K. et al. Reconstitution of membrane proteins in phospholipid bilayer nanodiscs. *Method Enzymol.* **464**, 211–231 (2009).
61. Rheinberger, J., Oostergetel, G., Resch, G. P. & Paulino, C. Optimized cryo-EM data-acquisition workflow by sample-thickness determination. *Acta Crystallogr. D. Struct. Biol.* **77**, 565–571 (2021).
62. Tegunov, D. & Cramer, P. Real-time cryo-electron microscopy data preprocessing with Warp. *Nat. Methods* **16**, 1146–1152 (2019).
63. Biyani, N. et al. Focus: the interface between data collection and data processing in cryo-EM. *J. Struct. Biol.* **198**, 124–133 (2017).
64. Zheng, S. Q. et al. MotionCor2: anisotropic correction of beam-induced motion for improved cryo-electron microscopy. *Nat. Methods* **14**, 331–332 (2017).
65. Rohou, A. & Grigorieff, N. CTFFIND4: fast and accurate defocus estimation from electron micrographs. *J. Struct. Biol.* **192**, 216–221 (2015).
66. Wagner, T. et al. SPHIRE-crYOLO is a fast and accurate fully automated particle picker for cryo-EM. *Commun. Biol.* **2**, 218 (2019).
67. Wagner, T. & Raunser, S. The evolution of SPHIRE-crYOLO particle picking and its application in automated cryo-EM processing workflows.*Commun. Biol.* **3**, 61 (2020).
68. Zivanov, J. et al. New tools for automated high-resolution cryo-EM structure determination in RELION-3. *eLife* **7**, e42166 (2018).
69. Punjani, A., Rubinstein, J. L., Fleet, D. J. & Brubaker, M. A. cryoSPARC: algorithms for rapid unsupervised cryo-EM structure determination. *Nat. Methods* **14**, 290 (2017).
70. Asarnow, D., Palovcak, E. & Cheng, Y. asarnow/pyem: UCSF pyem v0.5. *Zenodo* https://doi.org/10.5281/ZENODO.3576630 (2019).
71. Zivanov, J., Nakane, T. & Scheres, S. H. W. A Bayesian approach to beam-induced motion correction in cryo-EM single-particle analysis. *IUCrJ* **6**, 5–17 (2019).
72. Adams, P. D. et al. *PHENIX*: a comprehensive Python-based system for macromolecular structure solution. *Acta Crystallogr. D. Biol. Crystallogr.* **66**, 213–221 (2010).
73. Liebschner, D. et al. Macromolecular structure determination using X-rays, neutrons and electrons: recent developments in *Phenix*. *Acta Crystallogr. D. Struct. Biol.* **75**, 861–877 (2019).
74. Pettersen, E. F. et al. UCSF chimera - a visualization system for exploratory research and analysis. *J. Comput. Chem.* **25**, 1605–1612 (2004).

75. Emsley, P. & Cowtan, K. *Coot*: model-building tools for molecular graphics. *Acta Crystallogr. D. Biol. Crystallogr.* **60**, 2126–2132 (2004).
76. Croll, T. I. *ISOLDE*: a physically realistic environment for model building into low-resolution electron-density maps. *Acta Crystallogr. D. Struct. Biol.* **74**, 519–530 (2018).
77. Goddard, T. D. et al. UCSF ChimeraX: meeting modern challenges in visualization and analysis. *Protein Sci.* **27**, 14–25 (2018).
78. Morin, A. et al. Collaboration gets the most out of software. *eLife* **2**, e01456 (2013).
79. Lee, J. et al. CHARMM-GUI input generator for NAMD, GROMACS, AMBER, OpenMM, and CHARMM/OpenMM simulations using the CHARMM36 additive force field. *J. Chem. Theory Comput.* **12**, 405–413 (2016).
80. Mackerell, A. D., Feig, M. & Brooks, C. L. Extending the treatment of backbone energetics in protein force fields: Limitations of gas-phase quantum mechanics in reproducing protein conformational distributions in molecular dynamics simulations. *J. Comput. Chem.* **25**, 1400–1415 (2004).
81. Huang, J. et al. CHARMM36m: an improved force field for folded and intrinsically disordered proteins. *Nat. Methods* **14**, 71–73 (2017).
82. Klauda, J. B. et al. Update of the CHARMM all-atom additive force field for lipids: validation on six lipid types. *J. Phys. Chem. B* **114**, 7830–7843 (2010).
83. Jorgensen, W. L., Chandrasekhar, J., Madura, J. D., Impey, R. W. & Klein, M. L. Comparison of simple potential functions for simulating liquid water. *J. Chem. Phys.* **79**, 926–935 (1983).
84. Darden, T., York, D. & Pedersen, L. Particle mesh Ewald: an $N \cdot \log(N)$ method for Ewald sums in large systems.*J. Chem. Phys.* **98**, 10089–10092 (1993).
85. Hess, B., Bekker, H., Berendsen, H. J. C. & Fraaije, J. G. E. M. LINCS: a linear constraint solver for molecular simulations. *J. Comput. Chem.* **18**, 1463–1472 (1997).
86. Nosé, S. A unified formulation of the constant temperature molecular dynamics methods. *J. Chem. Phys.* **81**, 511–519 (1984).
87. Parrinello, M. & Rahman, A. Polymorphic transitions in single crystals: a new molecular dynamics method. *J. Appl. Phys.* **52**, 7182–7190 (1981).
88. Abraham, M. J. et al. GROMACS: High performance molecular simulations through multi-level parallelism from laptops to supercomputers. *SoftwareX* **1–2**, 19–25 (2015).
89. Tiwary, P., Limongelli, V., Salvalaglio, M. & Parrinello, M. Kinetics of protein–ligand unbinding: predicting pathways, rates, and rate-limiting steps. *Proc. Natl. Acad. Sci. USA* **112**, 386 (2015).
90. Brotzakis, Z. F., Limongelli, V. & Parrinello, M. Accelerating the calculation of protein–ligand binding free energy and residence times using dynamically optimized collective variables. *J. Chem. Theory Comput.* **15**, 743–750 (2019).
91. Capelli, R. et al. Chasing the full free energy landscape of neuroreceptor/ligand unbinding by metadynamics simulations. *J. Chem. Theory Comput.* **15**, 3354–3361 (2019).
92. Capelli, R., Carloni, P. & Parrinello, M. Exhaustive Search of Ligand Binding Pathways via Volume-Based Metadynamics. *J. Phys. Chem. Lett.* **10**, 3495–3499 (2019).
93. Tiwary, P. & Parrinello, M. A time-independent free energy estimator for metadynamics. *J. Phys. Chem. B* **119**, 736–742 (2015).
94. Tribello, G. A., Bonomi, M., Branduardi, D., Camilloni, C. & Bussi, G. PLUMED 2: new feathers for an old bird. *Computn Phys. Commun.* **185**, 604–613 (2014).
95. The PLUMED consortium. Promoting transparency and reproducibility in enhanced molecular simulations. *Nat. Methods* **16**, 670–673 (2019).
96. Marcos-Alcalde, I., Setoain, J., Mendieta-Moreno, J. I., Mendieta, J. & Gómez-Puertas, P. MEPSA: minimum energy pathway analysis for energy landscapes. *Bioinformatics* **31**, 3853–3855 (2015).
97. Iudin, A. et al. EMPIAR: the Electron Microscopy Public Image Archive. *Nucleic Acids Res.* **51**, D1503–D1511 (2023).

Acknowledgements

We want to thank T. Postmus for preliminary experiments with ASCT2 reconstitution into nanodiscs, M. König for initial help with MD simulations, M. Punter for maintenance of the image processing cluster, M. Stuart for assistance with cryo-EM, V. Kalienkova and C. Thangaratnarajah for their advice on image processing. We thank all members of Membrane Enzymology and Paulino lab for the helpful discussion. This work benefited from access to the Netherlands Centre for Electron Nanoscopy (NeCEN) at Leiden University, an Instruct-ERIC center, which was funded by the Netherlands Electron Microscopy Infrastructure (NEMI), project number 184.034.014 of the National Roadmap for Large-Scale Research Infrastructure of the Dutch Research Council (NWO). C.P. acknowledges funding from the Dutch Research Council: Nederlandse Organisatie voor Wetenschappelijk Onderzoek (NWO) Veni Grant 722.017.001 and NWO Start-Up Grant 740.018.016.

Author contributions

A.B., A.A.G., C.P., and D.J.S. designed the research. A.A.G. performed initial nanodisc reconstitution experiments. A.B. performed protein expression, purification, transport assay, and nanodisc reconstitution, acquired all cryo-EM, data, and determined all structures. J.R. assisted A.B. in collecting cryo-EM data. M.G.C. and S.J.M. performed molecular dynamics simulations. All authors analyzed data. A.B. and D.J.S. prepared the manuscript with input from all authors.

Competing interests

The authors declare no competing interests.

Additional information

Supplementary information The online version contains supplementary material available at https://doi.org/10.1038/s41467-024-50888-8.

Correspondence and requests for materials should be addressed to Cristina Paulino or Dirk J. Slotboom.

Peer review information *Nature Communications* thanks Noah Trebesch and the other, anonymous, reviewer(s) for their contribution to the peer review of this work. A peer review file is available.